THESIS FOR THE DEGREE OF LICENTIATE OF ENGINEERING

Role of nanopowder as sintering aid in the densification of water atomized ferrous powder

Swathi Kiranmayee Manchili

Department of Industrial and Materials Science
CHALMERS UNIVERSITY OF TECHNOLOGY
Gothenburg, Sweden, 2018

Role of nanopowder as sintering aid in the densification of water atomized ferrous powder

Swathi Kiranmayee Manchili

No. IMS-2018-20

Department of Industrial and Materials Science
Chalmers University of Technology
SE-412 96 Gothenburg
Sweden
Tel: +46 (0)31 772 1000

Printed by Chalmers Reproservice
Gothenburg, Sweden 2018

मूल श्लोकः

कर्मण्येवाधिकारस्ते मा फलेषु कदाचन।

मा कर्मफलहेतुर्भूर्मा ते सङ्गोऽस्त्वकर्मणि॥2.47॥

karmaṇyevādhikāraste
mā phaleṣu kadācana |
mā karmaphalaheturbhūḥ
mā te saṅgo'stvakarmaṇi |2.47|

-Bhagavad Gita

అమ్మ, నాన్న

Amma Nanna

Role of nanopowder as sintering aid in the densification of water atomized ferrous powder

Swathi Kiranmayee Manchili
Department of Industrial and Materials Science
Chalmers University of Technology

Abstract

Press and sinter powder metallurgy (PM) steels are cost-effective solutions for structural applications. There is a constant drive for the improvement in the density of these PM steels which helps in expanding their usage in applications demanding higher performance than what they deliver today. In press and sinter PM, consolidation is primarily achieved by compaction and sintering helps in bonding the powder particles metallurgically. One of the promising ways to achieve improved densification during sintering is through the addition of sintering activators to the conventional micrometer sized metal powder.

Nanopowder particles are associated with excess surface energy due to very high 'surface-to-volume' ratio. Therefore, there is an enhanced reactivity in this category of materials. Another consequence of the excess surface energy is the lowering of sintering temperature. For instance, powder blends containing micro and nano powders are known to yield high densities when processed through other manufacturing routes such as metal injection molding. In this thesis the possibility of achieving improved densification by means of nanopowder addition as a sintering aid is explored for the case of water atomized iron powder processed through the press and sinter route.

In this study, the influence of nanopowder addition on sintering of water atomised iron powder has been investigated. Before venturing into the sintering aspects, surface and thermal characteristics of nanopowder were investigated. X-Ray photoelectron spectroscopy (XPS) was used to evaluate the surface oxide thickness and composition of both iron and steel nanopowder. Different models were used for this purpose and the results were complemented by those obtained from thermogravimetric analysis. A methodology to measure the thickness of surface oxide on the nanopowder was thus proposed. Further, surface oxide reduction and possibility of melt point depression for the nanopowder was evaluated using thermal analysis.

For the sintering studies, various powder blends were prepared based on two different nano powder compositions, varying amounts of nanopowder content and with graphite addition to understand the influence of the individual constituents on the densification behaviour. Further, the blends were subjected to uniaxial compaction at varying pressures after which sintering was performed on the green compacts at varying heating rates. The presence and an increase in the amount of nanopowder decreased the compressibility of the blends. However, there was a clear influence of the nanopowder addition on the sintering behavior in the temperature regime as low as 500 to 700 °C when compared to compacts containing only micro-powder. To understand it further, sintering at intermittent temperatures and subsequent fractography were undertaken. It was found that the nanopowder sintering is activated at temperatures below 700 °C which contributed to the difference in sinter curve behaviour. Sinter response depended on the composition of the powder blend; however heating rate did not show much influence. An increase in the amount of nanopowder improved the density of the sintered compacts proportionally.

Keywords: sintering, nanopowder, surface oxide, thermal analysis,

PREFACE

This licentiate thesis is based on the work performed in the Department of Industrial and Materials Science at Chalmers University of Technology during June 2016 to October 2018. The work has been carried out under the supervision of Professor Lars Nyborg and Professor Eduard Hryha. This work has been performed within the framework of project funding from Swedish Foundation for Strategic Research.

This thesis consists of an introductory part with an emphasis on aspects related to sintering of PM steels and a summary of the work performed which is included in the following appended papers. The results section and the appended papers for the ease of understanding are divided into two categories- those with focus on powder characterization and the rest on sintering.

Powder characterisation

1. **Surface analysis of iron and steel nanopowder**
   Swathi K. Manchili, R. Shvab, A. Zehri, L. Ye, E. Hryha, J. Liu, L. Nyborg

   Surface and Interface Analysis, 2018, Vol. 50, ECASIA Special Issue, pp. 1083-1088

Sintering

2. **Effect of nanopowder addition on sintering of water atomized iron powder**
   Swathi K. Manchili, J. Wendel, A. Zehri, J. Liu, E. Hryha, L. Nyborg

   Manuscript, partly presented at International Conference on Sintering 2017, San Diego, USA

3. **Influence of iron nanopowder addition on sintering of water atomized iron powder**
   Swathi K.Manchili, J. Wendel, E. Hryha, L. Nyborg

   Proceedings of World Congress on Powder Metallurgy 2018, Beijing, China

Contribution to the appended Papers

I. The author planned the experimental work and wrote the paper with cooperation of the co-authors. XPS was performed by Dr. Ruslan Shvab. Analysis of results was performed by the author.

II. The author planned and executed the experiments. The author analysed the results and wrote the paper with the help of co-authors.

III. The author planned and executed the experiments. The author analysed the results and wrote the paper with the help of co-authors.

CONTENTS

1 Introduction

1.1 Background

Powder metallurgy (PM) is a manufacturing process in which powder is processed to produce components of various shapes. It can also be defined as a technology which involves converting starting material to powder, processing the powder to the required shape and making it useful for the application. The fluid like behaviour of powder helps in a variety of shaping processes. This is beneficial for forming many objects ranging from rocket parts to automotive parts and to pottery which can be produced through the PM route. After the shaping operation, the part is heated so that the metal particles bond to one another, which will impart strength. Though the shaping process transforms powder lot to net-shape, it is the sintering during which the particles bond and impart the desirable properties. Thus, the interest in studying sintering and understanding the underlying mechanism becomes crucial. Particles sinter-bond at relatively high temperatures. This means that sintering is carried out at temperatures above 0.5 T_m, where T_m refers to the melting temperature. The metal particles involved are usually in sizes less than 1 mm and have different shapes depending on the powder manufacturing process.

It is known that the particles of small sizes are associated with high surface energy-volume ratio, which means that the surface energy is relatively large. During sintering, reduction in the surface area with the formation sinter bonds between the particles reduces the excess surface energy. It is a solid-state process for most of the metals. Volumetric shrinkage during the sintering is accompanied with an increased density of the part. Properties like tensile strength, ductility, impact strength and fatigue strength are directly dependent on the density of the component, see Figure 1.

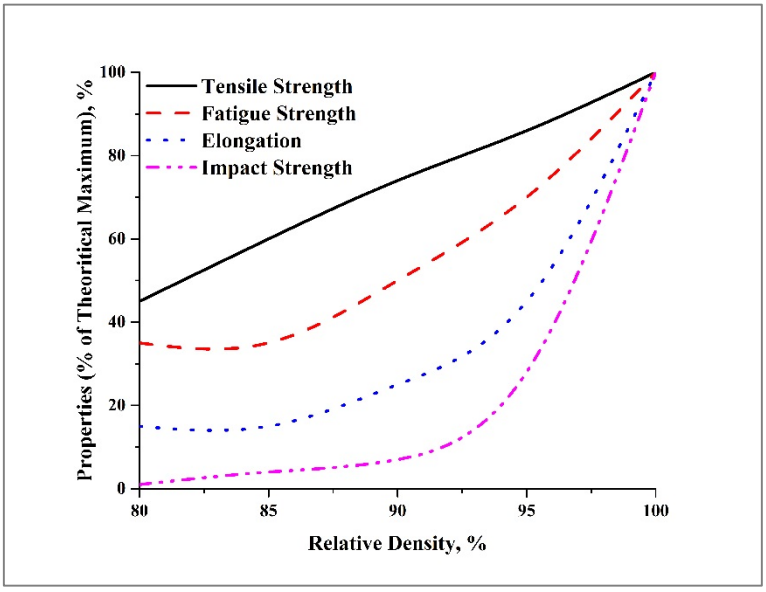

Figure 1: Representative graph showing the influence of relative density on the **mechanical properties of the part** [1].

For structural applications, components manufactured through PM route, improving the mechanical performance is of foremost importance as to ensure the growth and improve competitiveness with other manufacturing methods. From Figure 1, it is clear that the mechanical properties are a function of density therefore it is essential to improve the density of PM parts. For the PM steel components made through conventional press and sinter route, typical density obtained is in the range of 7.0 to 7.4 g/cm^3 which is less than 95% of the theoretical density. If this value is improved, then this will allow PM manufacturing to enter

new arenas of applications. Improvement of density can be either in the core or on the surface depending on the application. Overall improvement in the density opens up areas of application like high performance transmission gears in the automotive industry.

Predominant market for press and sinter structural PM components is in the automotive sector. On an average, around 80% of all the PM components for structural applications are used for automotive applications; of which the majority are used for transmission purposes [2]. The most common metal powder grades used comprise iron, steel, stainless steel of which iron powder is the most produced and consumed of the global powder metallurgy market [3]. Iron powder is produced mainly by reduction of iron oxide (providing so called sponge iron) and by means of water atomization. Water atomized and sponge iron powder are hence most commonly used powder for structural PM components.

1.2 Research Objective

The intention behind improving the density of PM parts is clear from the previous section. Broadly, the objective of the present study is to improve the density of water atomized iron powder components. There are different ways in which the density can be improved. Some of them are (a) employing high sintering temperature, (b) longer holding time at sintering temperature, and (c) using an aid to improve densification. Addition of a sintering aid is a known way to improve the density as seen in liquid phase sintering where an aid is added which melts and improves the density of the part. One of the possible ways to achieve improved densification during sintering is through the addition of nanopowder to the conventional micrometer sized metal powder. The objective of the present study is to clarify the role of nanopowder addition as sintering aid in the sintering of water atomized iron powder. Nanopowder is associated with enhanced surface energy which is expected to aid the sintering process. In this regard, the author intends to study the accelerated sintering process in the presence of nanopowder and a sintering study was hence formalized/formulated. Nanopowder is explored as an additive to conventional iron powder and the powder blend would be subjected to traditional PM route involving compaction and sintering. Prior to venturing into studying the influence of the nanopowder addition on sintering, a comprehensive study of the characteristics of nanopowder critical for sintering was considered essential. The questions can be formulated as

a. What is the surface chemistry of the nanopowder and how can it be determined?
b. What are the physical and chemical changes that can occur in the nanopowder when subjected to temperatures relevant for sintering?
c. How does the addition of nanopowder influence the uniaxial compaction behavior nanopowder?
d. What is the influence of nanopowder on the subsequent sintering process after compaction?

2 Powder Metallurgy

Powder is collection of particles which are generally bigger than an atom and smaller than 1 mm in size. If only powder is poured in to a container, it occupies the space in not a very efficient way. Only spherical metal particles with adapted particle size distribution can have a packing density of up to 64%. So, for efficient packing of powder, the shape and size of powder is crucial. In conventional press and sinter route, the powder is processed/converted in to required shape by application of pressure. This stage is called compaction and the resulting green compact has the shape but no strength to perform the intended application therefore necessitating a high temperature operation called sintering.

Before powder metallurgy (PM) turned into a mass production technology in 20th century, it is believed to have beginnings in 3000 B.C. The process of sintering has been known for thousands of years [4]. It was used to impart strength to bricks which is used till date for number of ceramics including porcelain, refractories, and bricks. Carburizing of iron and quenching technique was known to ancient Egyptians during 1200 to 700 B.C. Daggers with gold powder were found in Egypt during the 14th century B.C. Delhi iron pillar in India which weighs 6.5 tonnes approximately dates back to 300 A. D. This pillar was likely processed by hammering or forging reduced iron from iron ore. The PM principles were applied for processing platinum as well due to its high melting point. The modern renaissance of powder metallurgy can be traced to Coolidge, who used tungsten powder for lamp filaments to be used in electric lamp by Edison. Considerable development happened during the late 19th and early 20th century. Cemented carbides and porous bearings were developed. By 1940s nuclear fuel elements and many refractories were also manufactured using PM. Present day, PM is used in a wide of variety of applications ranging from dental implants to rocket nozzles and semiconductor substrates. The modern day applications depend mostly on manufacturing economy, improved properties and novel compositions. PM is useful for tailoring the composition in order to produce a variety of alloy systems to meet specific requirements [5]. It is worth pointing out that PM manufacturing is known to be sustainable owing to the very low material waste and high energy efficiency (Figure 2).

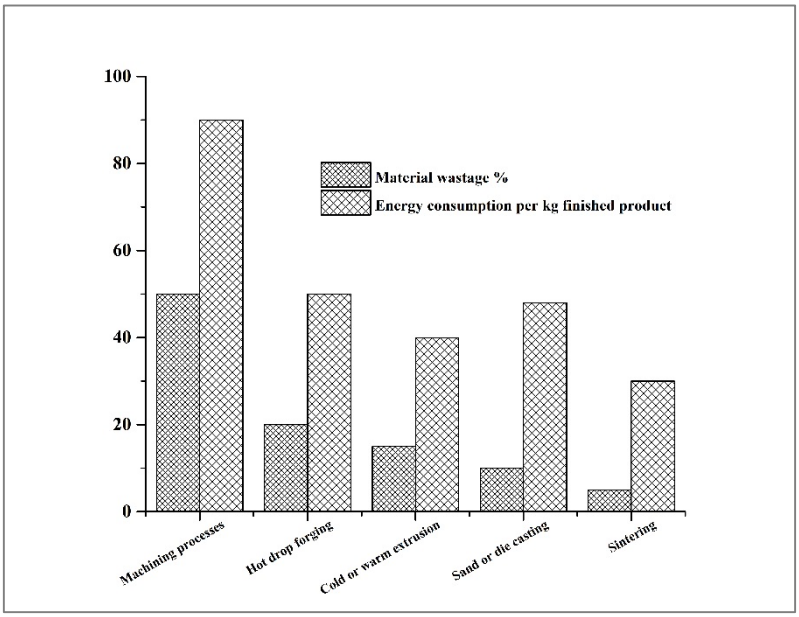

Figure 2: Economic considerations showing how powder metallurgical processing is a sustainable manufacturing technique. Redrawn from [2].

2.1 Different ways to achieve densification

The importance of density has been discussed in chapter 1. There are different ways to achieve densification. This means that the maximum densification is obtained during compaction or sintering. In conventional press and sinter process, maximum densification is obtained during compaction. The use of lubricant is a necessity in compaction and hence prior to sintering, so-called debinding is done. The following sintering imparts metallurgical bonds between the particles, adding strength to the part. In metal injection molding (MIM), metal powder is mixed with a binder and is injection molded. Green part is then subjected to significant binder removal and further to sintering. There is a considerable amount of shrinkage during this step owing to much finer powder size used. Therefore, the densification is from the sintering step in MIM. There are hybrid techniques like hot isostatic pressing where both pressure and temperature act at the same time and contribute to densification. Usually, the powder is filled into a metal container, which is evacuated and sealed prior to the hot isostatic pressing (HIP) process. The HIP cannot be considered as true sintering process since the densification is mostly carried by creep processes and only small amount of sintering in the last stage of densification.

In the above context, the current thesis attempts to study the possibility of incorporating a sintering based densification in an otherwise compaction based densification press and sinter through the utilization of sintering aid in the form of metallic nanopowder.

2.2 Process chart of powder metallurgy

There are different stages involved in the PM processing route. A typical press and sinter route, which is the focus of this thesis, is presented in the flow chart below, see Figure 3. The general sequence of events is: metal powder is blended with lubricant/additives and compacted to the required shape using cold or warm compaction. Warm compaction is when the compaction tool and powder are heated to a moderate elevated temperature at maximum 150°C [6]. The so called green compact is thereafter subjected to high temperature to impart necessary strength through sintering operation. After sintering, the component is subjected to secondary or finishing operations depending on the requirement. Each of these stages is explained below in detail.

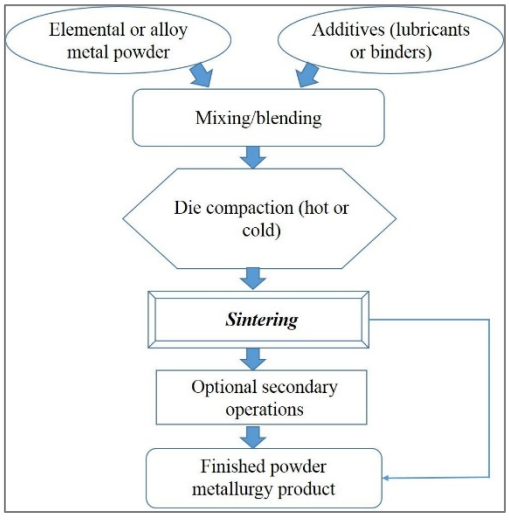

Figure 3: Process chart for powder metallurgy.

2.2.1 Production of metal powder

Metal powder, which is the raw material for the PM process can be manufactured through different ways. A material has to be supplied with energy in order to create new surfaces. For

the case of metal powder, therefore, the energy needed to create new surface is high and the process to create them should be efficient. For structural PM parts, the choice of powder manufacturing technology largely depends on the economic aspects and the required characteristics and desired application. Powder production technology can be broadly divided into 4 different types: mechanical, physical-mechanical, chemical and physical-chemical [7] [8].

Grinding, milling and mechanical alloying are considered to be mechanical processes for powder manufacturing. They are based on the principle of mechanical disintegration where the mechanical motion energy is used to create new surfaces. This is a solid state process where a fracture is initiated and propagated creating new surfaces. Mechanical disintegration can occur by different mechanisms like impact, shear, wear and pressure. In these processes, the smaller the particle, the more difficult it is to apply shear stress for further disintegration and also there is a probability for re-bonding as the energy associated with small particles is high. Generally, jaw crusher is used for grinding and ball mill is used for milling. Mechanical alloying is carried out in an attrition mill where generally a second phase is uniformly distributed in a metallic matrix. This means that the alloying is a result of repeated fracture and cold welding during which the second phase is dispersed.

Physical-mechanical methods include all atomization of melts. The principle is disintegration of molten melt stream by application of a gas or fluid jet [9]. Disintegrated drops of melt solidify rapidly during the flight due to rapid cooling-down. Various shapes of particles are obtained depending on factors like the melt temperature and viscosity and the cooling conditions. To obtain fine particles the viscosity of melt is generally decreased. Alloy powder can also be produced through this process; as rapid cooling is involved, it allows homogenous distribution of components of an alloy in particles. There are different types of atomization processes depending on the type of disintegrating medium used. Water atomization is when water jet is used to disrupt the melt stream [10]. Particles obtained through this route are irregular in shape and are high in oxygen content. The powder hence is usually subjected to a subsequent reduction annealing step. Water atomization is economical and has very high productivity. Gas atomization is when the melt stream is disintegrated by air, He, Ar or nitrogen which flow from the nozzles at a certain pressure. This method is recommended for highly alloyed materials like superalloys and stainless steels. The characteristic of gas-atomized powder is its spherical shape and homogeneity in chemical composition. Another form of atomization is centrifugal atomization (rotating electrode method) where an arc is struck between the alloy electrode which acts as an anode and water cooled tungsten electrode which is the cathode. So, it is a two-step process which involves melting of the alloy or metal and the centrifugal forces which disintegrate the molten metal or alloy [5].

Chemical production methods involve reduction of metal compounds like reduction of iron oxides to produce iron sponge powder, reduction of WO_3 to form tungsten powder, etc. Reduction process is significant as more than half of iron powder production for PM applications is through the reduction of iron oxide. Solid or gaseous reducing agents are used for the process and high temperature is employed. Depending on the reducing agent there can be either direct or indirect reduction reaction. Electrochemical production methods can be used for good number metals, where electrolysis is carried out to obtain metal powder from metals like Ni, Cu. Molten salts or water solutions are used as an electrolyte.

In this thesis study, iron or steel powder produced through the water atomization process is used as the base powder. The steel nano powder utilized in the study is produced through a proprietary process.

2.2.2 **Powder Shaping and Compaction**

Shaping of the powder into required shape can be achieved through pressure assisted compaction process. Powder mixed with additives is poured into the die cavity and is subjected to mechanical loading. The applied compaction pressure leads to the compaction of powder. There is friction between the metal particles and also between the metal particles and die walls. Additives in the form of lubricant are added to reduce the friction and improve the die life. When the compacting pressure is applied on the powder, first there is rearrangement which takes places by filling the cavities. As the pressure applied increases, the surface contact area increases and the particles are plastically deformed [11]. Depending on the shape of the particles, mechanical interlocking is also possible. Upon further increase in pressure, there is further increase in the contact area. The metal particles are deformed which makes it difficult to further increase the contact area as they are hardened. Density obtained depends on various factors like the size, shape and distribution of metal particles, their composition and the oxide layer on the powder surfaces.

Apart from die pressing, powder shaping can be done by extrusion, forging, rolling or hot/cold isostatic pressing. There are also methods like explosive compaction where powder is compacted by explosive detonation. This is a dynamic and high energy process where the mechanical properties of the components are enhanced. Another important shaping technique is powder injection molding (PIM), often referred to as metal injection molding (MIM) in case of metal powder. The MIM process offers a unique advantage over conventional press and sinter by producing products with precise dimensional tolerances. Secondary processing is generally not required for MIM components. The MIM is also considered as a high-volume manufacturing technology. Apart from the pressure assisted methods, there are also a few pressure-less shaping methods generally used for ceramics also applicable to metal powder. A slurry is made and methods like slip casting or freeze casting are used [9].

The powder mixes studied in this thesis have been subjected to uniaxial compaction before sintering (unless otherwise specified).

2.2.3 **Sintering**

Sintering is the next step after powder shaping. It is a process during which strength is imparted into the part by heating it to around 60 to 75 percent of the melting point temperature (in Kelvin degrees). It can be carried in a single step or as a multi-step process depending on the requirement. For press and sinter components, before sintering, the lubricant added should be removed for which a de-lubrication operation is carried out.

Sintering is discussed in chapter 3 in detail.

2.3 **Advantages associated with press and sinter powder metallurgy**

There must be a good reason for choosing this manufacturing process over the conventional wrought manufacturing processes. There are in fact several reasons as to why powder metallurgy is a preferred route over other manufacturing routes. While there is a broad classification, the most important ones are cost effectiveness and uniqueness of the process. Therefore the material costs are drastically decreased which indicates the outstanding cost effectiveness of the process. Below are a few advantages [12], [13], [14], [15].

- It is considered as a mass production technology with very high production rates where there is a huge potential for cost savings as the price per unit produced is low. Even complex parts can be processed in large volume
- PM is a near net shape forming process and the process produces very little scrap with high material utilization
- High dimensional accuracy helps in minimizing or avoiding the finishing operations in some cases, as closer dimensional control is achieved with very good surface finish
- Unparalleled flexibility in producing different shapes and compositions which are otherwise not possible with good repeatability. The powder can be suspended in a liquid and can be used for casting to give them a shape
- A wide variety of metals and non-metals can be processed. High melting point hard metals or refractory materials are popularly used for PM with less difficulty and less cost. Certain products like sintered carbides, porous bearings can be made only through this processing route
- Tailored properties can be obtained by using a variety of compositions. Desired mechanical and physical properties like density, hardness toughness, stiffness, damping, and specific electrical or magnetic properties along with application versatility. Consistent isotropic properties and dimensions are obtained along with good chemical homogeneity
- Economical process as the raw materials can be readily available. Skilled machinists are not required which lowers the labor cost
- PM components with controlled inter-connected porosity can be infiltrated with lubricants and used as self-lubricating bearings for special applications. Magnetic components can also be produced using PM technology

2.4 Limitations

In spite of the many advantages with PM, there are a few disadvantages ([14], [15], [16], [17])

- High cost of metal powder in comparison to that of raw material used for melting
- Storage of metal powder may be difficult in some cases as they tend to deteriorate
- Cost of tooling and equipment may be high if the production volume is low
- Restriction on the part size, as large shaped parts are difficult to process through PM process
- Low strength, ductility and fracture toughness in comparison with their wrought counter parts
- Health hazard due to fine powder being processed. It may cause potential workforce health problems as the atmosphere can be contaminated with fine metal powder
- Metal like Al, Mg, Ti and Zr in fine powder state are prone to explosion and fire hazard

2.5 Design Considerations for press and sinter PM Parts

PM route can be used to process numerous components but a few design considerations should be kept in mind while designing the components through PM. A few of them are mentioned below [18].

First and foremost is the ejection of the part from the die. The design should be in such a way that the part can be easily ejected from the die. Thin walls, sharp corners or narrow edges are to be eliminated as the powder flow into such spaces is difficult. Varying wall thickness can be advantageous. Holes at right angles to pressing are not advisable whereas holes in the direction of pressing are recommended. Undercuts are not advisable as ejection of the part can be difficult.

3 Sintering

As mentioned earlier, sintering is a thermal process during which the particles bond and strength is imparted to the part. A better understanding of the sintering process is expected to provide an insight into improving the product quality. Density is used as a measure for degree of sintering and is expressed as g/cm^3 or kg/m^3. Theoretical density of a material is when it is pore-free in nature.

3.1 Definitions of sintering

There are different ways in which sintering can be been defined. Sintering can be as (a) a thermal treatment to bond particles which ultimately improves the strength or (b) a thermal treatment for bonding particles into a coherent solid structure via mass transport events that often occur on the atomic scale [19]. In physical terms, as mentioned earlier, sintering can be defined as a thermal treatment for the particles to bond into a coherent, solid structure via mass transport events which occur on atomic scale. In mechanical terms, sintering is a thermally activated transition of powder or a porous system to a thermodynamically more stable state through decreasing the surface free energy. Sintering is an operation during which powder particles in a pre-shaped body obtain required physical-mechanical properties by changing the structure. Sintering can also be defined as a process by which the powder compact is transformed to a strongly bonded monolithic mass. It can also be expressed as a complex process during which particles undergo changes in shape and size when heated to sufficiently high temperature. During sintering, hence, there is a volumetric shrinkage which leads to densification, as the pore volume and size are reduced. For this shrinkage to occur there need to be either fine enough powder size or the aid of e.g. liquid phase, see further below. There is consequently a significant enhancement in the mechanical strength of the material. If unchecked or uncontrolled there will be grain coarsening up on further heating.

3.2 Types of sintering

There are different ways in which sintering is carried out. It can broadly be divided into solid state and liquid state sintering. Solid state sintering is when there is a direct contact between the particles and the overall contact area increases during the process. In liquid phase sintering, the presence of a liquid ensures adherence of the solid particles together. There are two forms of liquid phase sintering: persistent and transient. In persistent, at sintering temperature the solid is partly soluble in the liquid and the liquid formed solidifies on cooling down. In transient liquid phase sintering, a low melting point phase reacts with other materials and forms a new phase with no remaining liquid, therefore the name transient [20]. There are a few more types of sintering like high pressure sintering, reactive sintering, microwave sintering and spark plasma sintering.

The key parameters for sintering are temperature, vapor pressure, initial particle size, particle size distribution, heating rate, holding time, presence of agglomerates, green density, uniformity of initial microstructure, atmosphere, sintering aids along with the material as it determines the surface energy, atomic size, activation energy for diffusion and crystal structure.

3.3 Theory of sintering

This section presents an overview of the principles and mechanisms associated with sintering of powders. This section is summarized based on the work presented in the following references [21], [22], [23], [24], [25], [26], [27], [28], [29], [30], [31].

The important question is why do materials sinter or why do the pores reduce in size?

There must be some phenomenon happening at high temperature or a driving force present to 'steer' the metal particles to sinter. This driving force can be seen in two different ways. One is on a macroscopic scale, where the driving force for sintering is lowering the excess energy associated with the free surfaces of the metal particles. Powder is associated with high specific surface area, i.e., surface area per unit weight is larger in the case of powder when compared to a solid material. All the surfaces are associated with certain amount of surface energy. Therefore, the metal particles having a very high surface area are associated with excess surface energy. Given an opportunity, the system then tries to lower the surface energy and therefore, the macroscopic driving force for sintering is lowering of excess energy associated with the powder. This reduction in the excess surface energy can occur in two different ways:

I. Reducing the total surface area by increasing the average size of the particles (coarsening of the particles). Coalescence of fine particles results in reduction of total surface area but no strong bonds are formed during this process. Generally, this is observed in loose powder sintering. Mechanical strength thus obtained is also very low.
II. High energy solid-vapor interface is replaced by a low energy solid-solid interface (grain boundary formation). Strong bond is formed between the particles and the solid-vapor interface is replaced by a solid-solid interface by the formation of a grain boundary between them. There is an inter-particulate transfer of certain atoms resulting in a chemical bond.

Both may occur simultaneously or one can precede the other.

This can be explained using a simple model as shown in Figure 4.

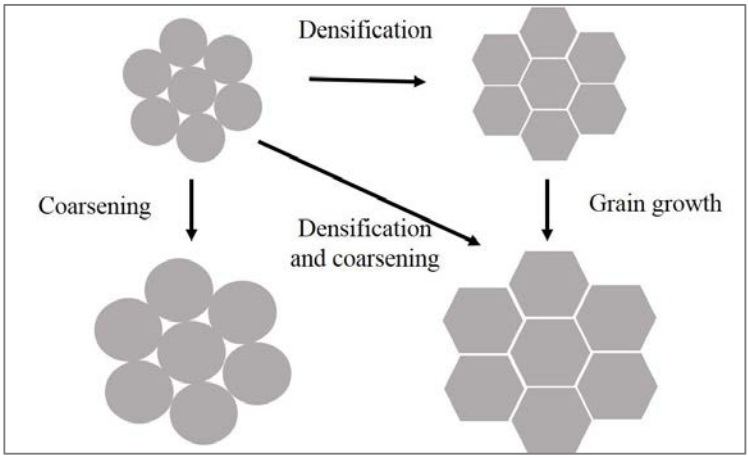

Figure 4: Schematic of particle coarsening and densification.

It can be seen from the figure above that in the initial condition when the particles are loosely bonded, the amount of solid-solid interface is much lesser in comparison to that of solid-vapor interface. There are three possibilities as to what can happen when the system is heated. One is the simple particle coarsening which was described above. Some of the particles grow at the expense of the others as the mass remains constant but the contact area does not change much as there is no chemical bonding. Therefore, there is a change in the surface area term. Overall energy of the system decreases as the surface energy term reduces but there is no strength imparted to the material. The other way is densification, particles change the configuration to form a strongly bonded structure by formation of the contacts and denser material is obtained. Strength is also imparted in this case. Surface energy term changes as the nature of surface is changed from solid-vapor to solid-solid contact. Both coarsening and densification can proceed

simultaneously, forming bonds and particles coarsening. A special case can exist when densification is followed by grain growth when sufficient energy is supplied. A relationship between pore size, grain size and theoretical density can be obtained from the above mentioned phenomena. Avoiding coarsening before sintering should be the objective.

An important condition for sintering to proceed from surface energy point of view is that the grain boundary energy or solid-solid interface energy should be less than twice the solid-vapor interface energy (Figure 5). When two surfaces are in contact with each other, there is a dihedral angle (Φ) which forms between the tangents drawn from the solid-solid interface. This angle should be less than 180° for sintering to take place. During the sintering process, a part of the surface is exposed to vapor phase and slowly this is eliminated by the development of a solid-solid interface. Tangents are drawn to the radius of curvature along which the solid-vapor surface acts. Normally, in metal powder the dihedral angle is around 120 °.

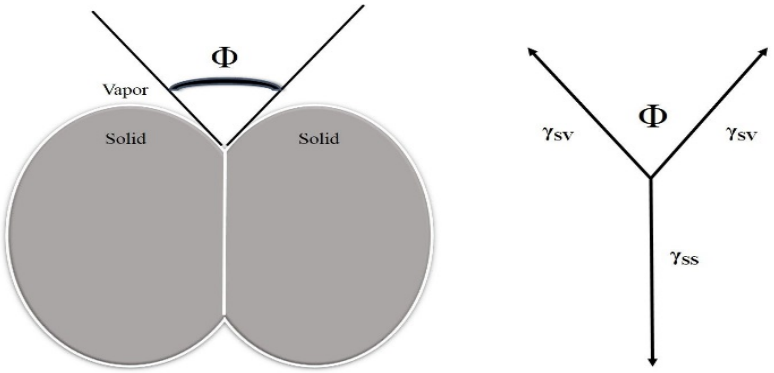

Figure 5: Schematic of how the dihedral angle is defined in terms of surface energies as the grain boundary emerges at the free surface (Redrawn from [32]**).**

For equilibrium conditions

$$\gamma_{gb} = 2\gamma_{sv} cos\frac{\emptyset}{2} \qquad \textbf{Equation 1}$$

In the case of liquid phase sintering, the same expression can be used but the solid-vapor interface is changed with solid-liquid interface.

What happens during sintering?

Sintering is the result of mass transport at atomic level; or in other words, the movement of atomic species from one site to another. There are different ways in which mass transport occurs, of which, solid state diffusion is the important one along with the vapor phase transport which is evaporation and condensation and occurs under certain conditions during sintering.

It has been stated earlier that the global driving force for sintering relates to the reduction in excess surface energy. There must be a local driving force as well for the mass transport to occur at the local level. It is known that the driving force for diffusion is the concentration gradient whereas the gradient of vapor pressure for vapor phase transport. It is essential to understand what sets up these gradients at the local level. In this context, the curvature of the particle plays a crucial role in realizing these gradients.

Point defects such as vacancies also play a pivotal role in diffusion mechanisms for mass transport which means that diffusion in a solid primarily occurs by point defects of which vacancies are the most important. Diffusion takes place when there is a concentration gradient and takes place through vacancy movement. Vacancies are introduced either by increasing the

temperature or by doping. Vacancy concentration changes as there is change in the radius of curvature. It is important to know how the vacancy concentration and vapor pressure vary as a function of curvature of the solid.

The potential difference between curved and flat surfaces leads to (a) difference between vapor pressure over these surfaces and (b) vacancy concentration difference just below these surfaces.

To understand the influence, it essential to formulate equation which speak about relationship between the curved surface and flat surface partial pressure over curved and flat surfaces.

Curvature dependent vapor pressure can be expressed as

$$\boldsymbol{P_c = P_f(1 + r_c \frac{V\gamma_{sv}}{kT})} \qquad \textbf{Equation 2}$$

Where P_c and P_f are the partial pressures over the curved and flat surface respectively, k is the Boltzmann constant, V is the volume and r_c is the radius of curvature of the solid surface. In the case of a sphere, $r_c = 2/r_o$ and T is the temperature. This is a relationship between the partial pressures of curved and flat surfaces.

For a flat surface, $r_c = 0$ then $P_c = P_f$

For a concave surface, r_c is negative then $P_c < P_f$

For a convex surface, r_c is positive then $P_c > P_f$

The above statements mean that a convex surface has a higher vapor pressure than that of a flat surface while a concave surface has a lower vapor pressure in comparison to the flat surface. For a spherical surface, vapor pressure is the same everywhere but in an agglomerate they have different surfaces at different points i.e., at a few locations it can be positive and at a few it can be negative and this difference contributes to the local driving force.

Activation energy is required for any defect formation. Energy required at flat and curved surfaces are different. Therefore the enthalpy associated in creating vacancies at flat and curved surfaces is also going to be different. Energy at different surfaces is different and the vacancy concentration just beneath it is different. Therefore, the concentration just below the surface will be different. An expression can be derived for a relationship between vacancy concentration for a curved and the flat surface energy and it is given by

$$\boldsymbol{C_{v(curve)} = C_o(1 - \frac{r_c V\gamma_{sv}}{kT})} \qquad \textbf{Equation 3}$$

Where $C_{v(curve)}$ is the vacancy concentration for a curved surface.

For flat surface, it is known that r_c = 0, then $C_v \sim C_o$ which is for flat surface.

For a convex surface, r_c is positive, $C_{v(convex)} < C_{v(flat)}$

For a concave surface, r_c is negative, $C_{v(concave)} > C_{v(flat)}$

Curvature dependent properties

- Vapour pressure : $P_{convex} > P_{flat} > P_{concave}$
- Vacancy concentration: $C_{v(concave)} > C_{v(flat)} > C_{v(convex)}$

Therefore, Eq. 2 and 3 describe the relation between the curvature of the particle and material movement.

Stages of sintering

Sintering is a temperature and time dependent phenomenon and densification is a result of it. Sintering kinetics are different during different stages of sintering and different atomic mechanisms of mass transport are active at different stages of sintering. This process can be categorized into three different stages based on pore shape and size.

Initial stage: contact area between the particles increases by neck growth.

Intermediate stage: Longest stage of sintering during which the relative density increases. Pores are continuous in nature.

Final stage: Continuous pores become isolated pores.

Mechanisms of mass transport during solid state sintering are as follows: evaporation and condensation, diffusion by vacancy mechanism and viscous flow (creep). Below, each of these is shortly described.

Evaporation and Condensation

The driving force is the difference in vapor pressure between the convex and concave surfaces. This can be explained by means of Figure 6. The two spherical particles uniform in size are in contact when a conglomeration of particles are compacted. Therefore, there are 2 surfaces created, that is, at the point contact there is a small concave surface and away from the contact there is convex surface. Therefore, a difference in vapor pressure between the surfaces creates a vapor pressure gradient. More vapor pressure is present on the convex surface in comparison to concave, so more material is evaporated from the convex surface and is transported to the concave surface and the material is condensed. This is because of the curvature but not owing to temperature gradient. As more and more material evaporates and condenses in concave area, neck area increases and the concave region becomes flatter. During this process, the distance between the centers of the neighboring particles does not change which means the overall dimension will not change or no shrinkage/densification is observed. Rate equation can be written for the evaporation and condensation mechanism which helps in predicting the rate of neck growth which is initially very high and then slows down (time dependency). The neck growth decreases with an increasing particle size (size dependency) and increases with an increase in vapor pressure of the solid.

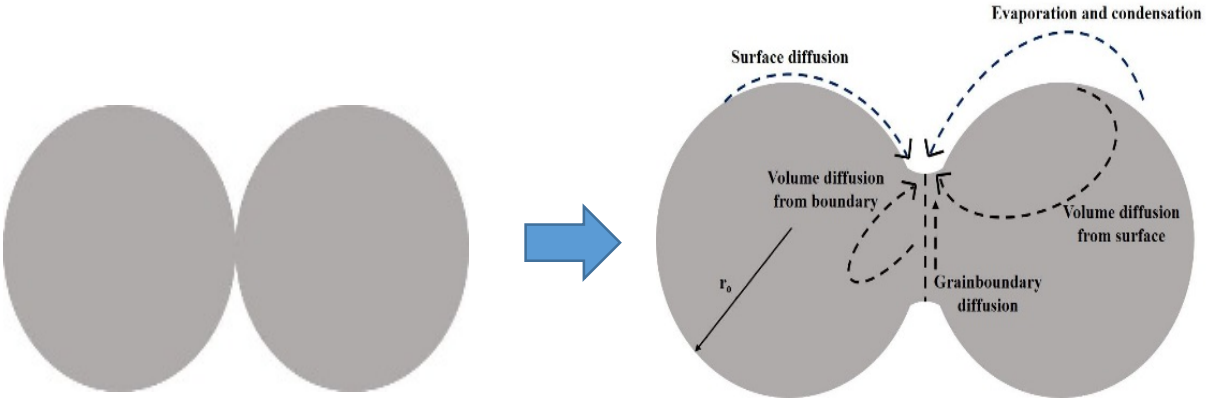

Figure 6: Schematic of different sintering mechanisms (redrawn from [33]**).**

Vacancy mechanisms of solid state sintering

As it is already known that the vacancy movement is driven from the concave surface to convex surface. As seen from Figure 6, vacancy moves from concave to convex surface so the material flow is in the opposite direction as the void will be filled up. Mass transport is the opposite in the case of vacancy mechanism in comparison to vapor transport mechanism. The movement of vacancies can take place in three different ways or three different paths are used.

Lattice/volume diffusion: the vacancies which are generated in the concave surface are moved to convex surface through the lattice or bulk of the material.

Surface diffusion: When the vacancies move along the surface or close to the surface.

Grain boundary diffusion: Vacancies move from concave to convex surfaces and also to flat surface which is the grain boundary between the adjacent particles.

The rate at which the above mentioned diffusion takes place is different for the different mechanisms. As a result of vacancy mechanism, unlike evaporation and condensation, there is shrinkage or change in dimension except in the case of surface diffusion.

Activation energy for surface diffusion is the lowest among the three diffusion paths, grain boundary is intermediate and lattice diffusion is the highest. Accordingly, surface diffusion is dominant at lower temperature while lattice diffusion at higher temperature. In smaller particle sizes, surface and grain boundary diffusion are preferred paths of diffusion. Lattice diffusion dominates for larger particle size, at longer times and at high temperatures.

The assumption that there is always a driving force to shrink the size of the pore throughout the course of sintering is not always true, as under certain conditions, the pores become thermodynamically stable. Pores get entrapped within the grains and thereby it is difficult to achieve theoretical density within a finite time. During the final stage of sintering, grain coarsening occurs along with pore elimination as the average grain size increases with time. Larger grains grow at the expense of the smaller ones. Hence, in practice, the shrinkage during solid sintering requires fine enough powder size, which is one main reason why normal water-atomized or sponge iron powder, having median size in the range of 50-100 μm, will show very small shrinkage if any during sintering.

3.4 Nanopowder sintering

To improve the density of water atomized iron powder in order to expand the application spectrum, nanopowder can be used as a sintering additive. During the sintering of the mixed powder, nanopowder could either show liquid-like sintering behavior [34] or sinter at low temperatures and contribute to densification in this respect [35].

Nanoscale materials are of interest owing to their modified solid-state properties compared to conventional solids [34]. One of the most interesting aspect concerning nanopowder is the dependence of melting point on the particle size [36]. Early thermodynamic model was developed in 1909 to predict a melting point depression of nanomaterials and it was found that the melting point temperature varied linearly with an inverse particle size [37]. Subsequently, research has been carried out to study the variation in melting temperature depending on the particle size on metals like gold, silver, tin, indium, lead and aluminum [38]. Techniques like scanning electron diffraction, transmission electron microscopy, X-ray diffraction and calorimetry have been used to investigate the depression in melting point [39]. This dependency is more prominent in the lower end of the size regime in comparison to large size regime [40].

Ultrafine particles like nanopowder with a diameter in the order of 10’s of nanometers has been of interest for research for quite some time now. This interest could be attributed to the unique

physical and chemical properties associated with nanopowder in their ultra-dispersed state [41]. Sintering is a promising way of preparing bulk materials using nanopowder. There is a metastable nature associated with nanopowder. This comes under the category of morphological metastability according to the Turnbull classification of metastability. The other ones being compositional, associated with extended solution ranges and structural or topological associated with crystal structure or phases [42]. Nanopowder exhibits isotropic shrinkage and possess low activation energy for sintering, therefore decreasing the sintering temperature is a representative advantage of nanopowder [43] [44]. Some additional challenges that accompany nanopowder in comparison with those of regular micrometer sized powder are particle agglomeration, inherent contamination, enhanced chemical reactivity and loss of the nano characteristics. Sintering mechanism for nanopowder may or may not be the same in comparison with the regular powder. There could be a new phenomenon in play. Nanopowder sintering presents additional challenges in the form of particle agglomeration, high reactivity, grain coarsening and ultimate loss of nano features [42]. Also, other drawbacks with the nanopowder are their high cost and low formability. An effective solution thus is to use a combination of nanometer and micrometer sized powder. One significant advantage of addition in such case of nanopowder is activated sintering [45].

Sintering micro-nanopowder mixture has previously been studied in the case of metal injection molding (MIM). The MIM is an attractive cost effective mass production technology utilized to manufacture net-shaped complex components [46]. It is a combination of injection moulding process and powder metallurgy. In the aforementioned study, densification of the micro-nanopowder mixture was observed to start below 800 °C and decreased with increasing fraction of nanopowder in the mixture [45] which is due to the low sintering activation energy attributed to the excess surface energy of the nanopowder [44] . It was observed that the relative sintered density of the micro-nanopowder compact was higher than that of the micro-powder compact alone [45]. There is a significant difference between the relative sintered density of micro-nanopowder compact and micro-powder compact in the relatively low temperature range (1000 °C) (because of denser grain boundary caused from sintered nanoparticles around the micro-powder which provide high diffusion paths) and after which the effect of nanopowder is dwindled and the micro-powder compact density is increased [35]. Joon et.al., observed that the relative sintered density increased from 73 to 90 % between the temperature range of 800 to 900 °C in micro-nano-powder MIM compact [35]. Similar behavior was observed in press and sintered 316 SS steel micro-nanopowder compacts [47].

3.4.1 **Mixing of powder**

Mixing of powder is of utmost importance in powder metallurgy industry as to ensure the repeatability of properties. The main problem is mixing and simultaneous deagglomeration of fine particles as they naturally tend to agglomerate. However, the high chemical reactivity and attraction due to the surface energy makes them attractive to use [48]. High energy and forces are applied to break down the agglomerates and to mix them. Ball milling is performed to grind fine powder and balls are chosen according to the material supposed to be ground [49]. Deagglomeration and mixing being the prime motive of the present study ball milling was not performed. It was seen in alumina and zirconia systems that bimodal ball size distribution helps in deagglomeration and mixing simultaneously [49].

4 Materials and Methods

The main objective of this thesis study has been to better understand the influence of nanopowder addition on the sintering behavior of micrometer-sized powder; for which water atomized iron powder served as a base powder. To the base powder, nanopowder was added and mixed, whereafter the mixture was compacted and sintered. For better understanding of the influence of nanopowder on the sintering, surface characterization of nanopowder was performed by means of X-ray photoelectron spectroscopy before proceeding with sintering studies, which in turn were performed utilizing a dilatometer. In addition, thermal analysis and electron microscopy were also performed.

4.1 Materials

Water atomization is a widely used process for the commercial production of metal powder in large tonnage. A falling stream of liquid metal is impinged by jets of water, which disintegrates the liquid stream into droplets. These are frozen immediately and form granules or powder. With high pressure water atomization it is viable to achieve fine particle size distribution. In principle, this technology could be used for all the metals that can be melted but is commercially available only for iron, copper, steels, aluminum, tin, lead. Examples of commercial products manufactured from water-atomized powder are iron powder for conventional press and sinter components, fine powder for metal injection molding and copper powder for bronze bearings. This process comes along with the challenge of oxidation, especially, for alloys which contain elements with high oxygen affinity [50]. Oxidation is also observed on the surface of the powder particles in the form of surface oxides. Elements like silicon, manganese and chromium in the liquid metal are sensitive and form oxides. Researchers analyzing stainless steel found that the surface oxides were rich in Fe, Cr, Mn and Si [51]. Generally, annealing is carried out to reduce the oxides content on the particle surfaces for iron and steel powder. The shape of the powder through water atomization is generally irregular unlike the spherically shaped particles through gas atomization (gas is used as a medium to disintegrate the liquid stream). For press and sinter parts, shape of the particle is of importance as the green strength of irregular shaped particles is higher than that of the spherical ones due to the mechanical interlocking between the particles.

For the base material in the present study, water-atomized iron powder was used. It is a commercially available powder grade with a trade name ASC, produced by Höganäs AB, Sweden. The powder sieved to <45 µm was used. The particle size distribution is shown in Figure 7 and the composition is given in Table 1.

Table 1: Composition of ASC 300(-45 µm) iron powder

Elements	C	O	Mn	Si	Cr	S	Sn	Fe
wt %.	0.0048	0.114	0.087	0.004	0.056	0.0093	0.003	Rest

The oxygen present in the powder is bound in the form of oxides on the surface or in internal inclusions in the matrix of the particle. A very small amount of oxygen is present in the elemental form in the iron matrix as it is well known that the solubility of oxygen is low in iron matrix. The morphology of the particles was irregular, characteristic of water-atomized powder and a few fine particulate oxides were observed on the surface (Figure 8), while the dominant part of water-atomized iron powder like the ASC grade is covered by thin (<7 nm) Fe-oxide layer [11].

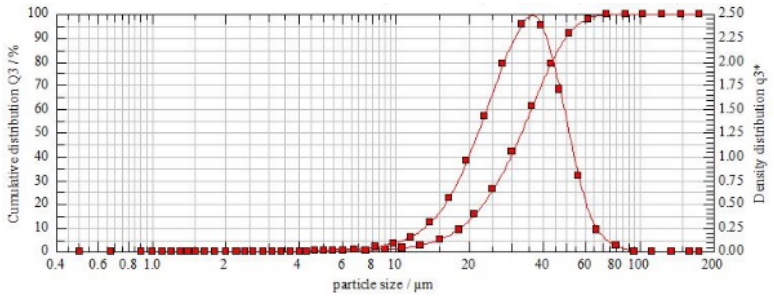

Figure 7: Particle size distribution of ASC 300 (-45 µm) water atomized iron powder.

4.1.1 Nanopowder

Steel nanopowder was used as an aid for the sintering process. An in-house technology, developed at Department of Microtechnology and Nanoscience by Prof. J. Liu and co-workers, was used to produce nanopowder used for the study. Steel nanopowder of the composition given in Table 2 was produced and supplied for the thesis study. The size of the steel nanopowder ranged from submicron to a few nanometers. During the processing of nanopowder, they come in contact with water after which they are dried. This leads to formation of thicker oxide scale on the nanopowder than found naturally on iron/steel surface, see Paper I. This steel nanopowder was used for the surface chemical characterization as well as an aid for the sintering.

Table 2: Composition of the steel rod used for producing the nanopowder

Elements	C	Mn	Si	S	P	Fe
wt %.	0.16-0.24	1.30-1.60	0.10-0.40	0.06 max	0.06 max	Rest

To serve as a reference, pure iron nanopowder was procured from Sigma-Aldricht Inc. Three different size fractions, namely 35-45, 40-60 and 60-80 nm, were purchased. These were supplied in sealed bottles by the manufacturer in dry state. Morphology of the iron nanopowder was spherical and the size was less than 100 nm on an average (Figure 8). Storing and handling of the powder was performed in a nitrogen filled glove box. Preparation of the samples for different characterization techniques was also carried out in the glove box under nitrogen atmosphere (99% purity). Transfer of the sample from the glove box to different equipment was done with utmost care. There was no explosive oxidation occurrence when the nanopowder or the steel nanopowder were exposed to the atmosphere.

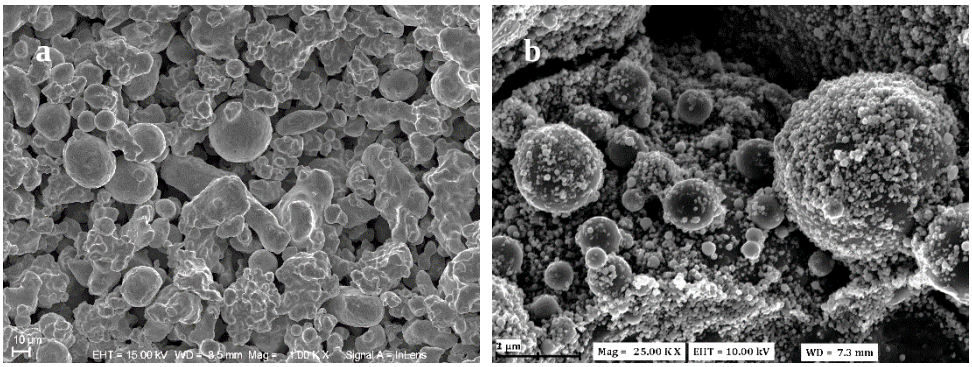

Figure 8: SEM micrographs showing morphology of (a) ASC 300 (-45 µm) iron powder [11] **and (b) nanopowder mixed with ASC 300 (-45 µm) iron powder**

4.1.2 **Mixing of the powder**

The nano and micrometer-sized powder were mixed using a tumbler placed in the glove box first and then with the lubricant before the compaction procedure. ASC (-45 µm) and pure iron nanopowder were mixed in different proportions whereas ASC (-45µm) and steel nanopowder were mixed only in a ratio of 95 wt.% and 5 wt.%, respectively. Carbon in the form of graphite powder was also added to some of the powder blends to study the influence of carbon on sintering. A second set of powder blends were made with varying nanopowder content. Details of different mixes used for compaction are listed in Table 3.

Table 3: Different powder blends

Powder blend composition (different composition)	**Powder blend composition (Varying amount of nanopowder)**
ASC 300 (-45 µm) + 5 wt. % Fe nanopowder	ASC 300 (-45 µm) + 5 wt. % Fe nanopowder
ASC 300 (-45 µm) + 5 wt. % Fe nanopowder + 0.4 wt. % C	ASC 300 (-45 µm) + 10 wt. % Fe nanopowder
ASC 300 (-45 µm) + 5 wt. % Steel nanopowder	ASC 300 (-45 µm) + 15 wt. % Fe nanopowder
ASC 300 (-45 µm) + 5 wt. % Steel nanopowder + 0.4 wt. % C	ASC 300 (-45 µm) + 20 wt. % Fe nanopowder

4.1.3 **Compaction**

Powder blends with different composition was compacted at Höganäs AB and were mixed with 0.6 wt.% LubE for lubrication. The powder blends were compacted using a compaction press under uniaxial loading conditions. Compaction pressures of 400, 600 and 800 MPa were employed. Cylindrical samples of 13.5 to 14.5 mm height and 11.5 mm in diameter were compacted from the powder blends. In-house compaction at Department of Industrial and Materials Science was carried out on the powder blends with varying amounts of nanopowder, which yielded in samples of the size of 10 mm diameter and 3.5 to 4.5 mm height. No lubricant was used for in-house compaction and compaction pressure used was approx. 550 MPa.

4.2 **Analytical Techniques**

4.2.1 **Thermogravimetry**

Thermogravimetry (TG) is a technique in which mass of a sample is monitored in a specified atmosphere against temperature and time [52]. The TG is also referred to as thermogravimetric analysis (TGA). During TGA, the sample is heated according to the specified temperature profile and the changes are recorded as the sample mass changes. It could be either mass gain or loss as the temperature is increased in a specified atmosphere. The mass of the sample is measured before the analysis and the relative mass change is recorded during TGA. Therefore, the equipment consists of sample holder, furnace, high resolution balance, vacuum system and thermocouple. The derivative of thermogravimetric curve is the rate of mass change with respect to time, $\Delta m/dt$ (Figure 9).

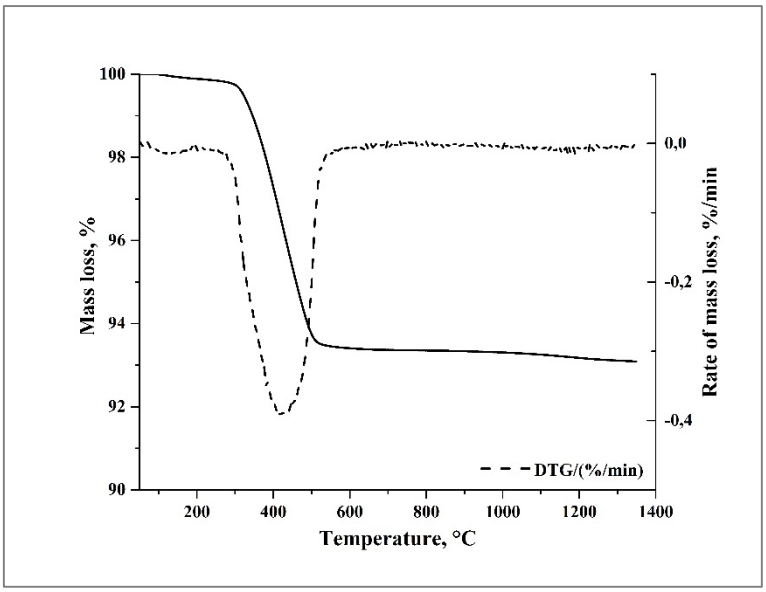

Figure 9: Thermogravimetry of iron nanopowder showing the mass loss and also the rate of mass loss for iron nanopowder.

The equipment used in the present study is STA449 F1 Jupiter (NETZSCH Thermal Analysis GmbH, Germany). It is a top loading system with an ultra-nano balance with a resolution of 25 ng. A W/Re thermocouple was used for the measurement of temperature. Alumina crucible was used as a sample carrier. Before starting the experiment, after loading the sample, the system was evacuated and purged with argon three times to ensure the atmosphere is good enough for the experiment. The furnace was evacuated and filled with argon for three times to ensure that the atmosphere is clean for the usage of hydrogen.

All the TGA experiments were carried out in a pure hydrogen atmosphere. Commercial iron nanopowder was evaluated using TGA. The samples were heated to 1350 °C at different heating rates like 5, 10 and 30 °C/min in pure hydrogen environment to ensure complete reduction of the surface oxide on the nanopowder. Though utmost care was taken in handling the nanopowder during the sample preparation and transfer there is a chance of reaction with the atmosphere oxygen. Sample storage and preparation were carried out in the glovebox for both DSC and TG analysis. The amount of iron in the nanopowder was calculated by considering the mass loss, total mass of the sample and the molecular weight of Fe_2O_3 and atomic weight of Fe. Flow rate of 100 ml/min was maintained throughout the process.

4.2.2 **Differential Scanning Calorimetry**

A calorimeter is used to measure the heat in or heat released or absorbed by a sample during controlled temperature program. Differential scanning calorimetry (DSC) is used for measuring the amount of energy absorbed or released by the sample when it is heated or cooled, where a sample and reference are used. It provides the data on the endothermic (heat absorption) and exothermic (heat evolution) processes. The DSC is used to measure melting temperature, heat of fusion, reaction energy and temperature, glass transition temperature, phase transition temperature, specific heat or heat capacity, etc. Heat is supplied to the sample and reference and the corresponding change in temperature is recorded depending on the radiated or absorbed heat by the sample. In a simple setup, energy is introduced into sample and the reference whose temperature is raised identically over the time. The sample absorbs or releases energy

depending on the endothermic or exothermic process respectively. Variety of pans as e.g. Al, Cu, Pt, alumina, etc., are used and depending on the material and temperature of analysis the crucibles are chosen. Sample is placed in the crucible and the reference crucible is left empty. Different gases like nitrogen, air, oxygen, argon can be used as process atmosphere for the analysis. Based on the mechanism of operation, DSCs are of two types: heat flux DSC and power compensated DSC. In a heat flux DSC, the sample pan and reference pan are placed inside a furnace which is heated at a preset heating rate and the heat is transferred to the pans through a thermoelectric desk. In a power compensated DSC, the sample and reference are placed in separate furnaces heated by separate heaters. The sample and reference are maintained at the same temperature and the difference in thermal energy required maintaining them at the same temperature is measured (Figure 10).

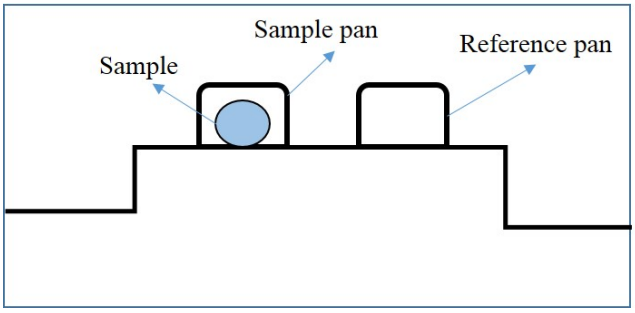

Figure 10: Ray diagram of DSC.

In the present study, a simultaneous thermal analyzer STA449 Jupiter F9 (NETZSCH Thermal Analysis GmbH, Germany) with a combined TG/DSC sensor with the S-type thermocouple was used to measure the phase transitions and melting temperatures of different nanopowder. It is a top-loading system with enthalpy accuracy of ±2%. Alumina crucible and argon atmosphere were used for all the analysis. The DSC experiments were carried out at 1450 °C at a heating rate of 10 °C/min.

4.2.3 **Dilatometry**

Dilatometry is a technique used for characterizing dimensional changes in a material as a function of temperature by means of measuring axial shrinkage or expansion as a function of temperature and time. The data generated is in the form of curves of dimension against time and temperature [53], see Figure 11. It can be used to perform rate-controlled sintering studies in powder metallurgy apart from studying the thermal expansion in materials. The push-rod dilatometer is used for the above mentioned purpose. For performing the analysis, the sample is placed in the sample holder region and the push rod is positioned directly on to the specimen. This pushrod helps in transmitting the dimensional change during the temperature program. This pushrod is a frictionless sensing rod in the center of a furnace tube. The temperature program is controlled by a thermocouple placed close to the sample. Linear variable displacement transducer is used as a sensing element for the length change.

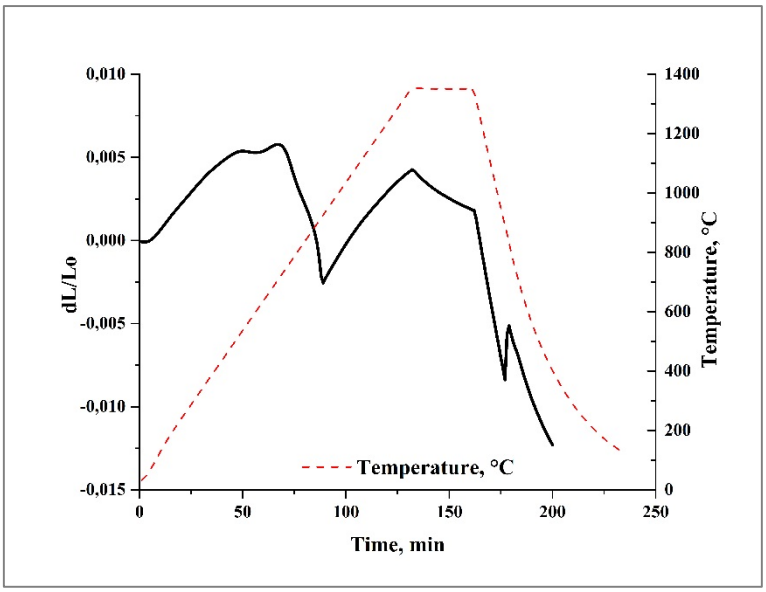

Figure 11: Dilatometry curve showing the sintering behavior of a powder blend compact.

A horizontal pushrod dilatometer DIL402C (NETZSCH Thermal Analysis GmbH, Germany) equipped with a vacuum furnace was used. All the dilatometry experiments were carried out in pure hydrogen (6N purity) atmosphere. The furnace was evacuated and purged with argon 3 times before the commencement of the sintering experiment to ensure the atmosphere is contaminant free. The details of the experiments are given in Table 4. Holding time of 30 min at the sintering temperature and a cooling rate of 30 °C/min were employed for all the sintering experiments.

Table 4: Sintering cycle

Powder blend composition	**Sintering parameters**	
Different composition	**Sintering temperature (° C)**	**Heating rate (°C/min)**
ASC 300 (-45 µm) + 5 wt. % Fe nanopowder	1350	5, 10, 30
ASC 300 (-45 µm) + 5 wt. % Fe nanopowder + 0.4 Wt. % C	1350	5, 10, 30
ASC 300 (-45 µm) + 5 wt. % Steel nanopowder	1350	5, 10, 30
ASC 300 (-45 µm) + 5 wt. % Steel nanopowder + 0.4 Wt. % C	1350	5, 10, 30
Varying amounts of nanopowder	**Sintering temperature (° C)**	**Heating rate (°C/min)**
ASC 300 (-45 µm) + 5 wt. % Fe nanopowder	500, 700, 900, 1100, 1350	10
ASC 300 (-45 µm) + 10 wt. % Fe nanopowder	500, 700, 1350	10
ASC 300 (-45 µm) + 15 wt. % Fe nanopowder	500, 700, 1350	10
ASC 300 (-45 µm) + 20 wt. % Fe nanopowder	1350	10

4.2.4 **X-ray Photoelectron Spectroscopy**

X-ray photoelectron spectroscopy (XPS), also known as electron spectroscopy for chemical analysis (ESCA) is the most widely used technique for surface analysis which provides both quantitative and chemical state information and can be applied to a broad range of materials. The sample surface is excited using e.g. mono-energetic AlK_α radiation causing photoelectrons to be emitted due to the photoelectric effect. Such soft X-rays are used for the analysis and the analysis is carried out in an ultra-high vacuum setup [54]. The kinetic energy of the emitted photoelectrons is analysed by means of a hemispherical analyzer. The binding energy (BE) based on the kinetic energy (KE) and photon energy ($h\vartheta$) equation is calculated as follows:

$$\boldsymbol{BE = h\vartheta - KE - \phi} \qquad \textbf{Equation 4}$$

The term $\boldsymbol{\phi}$ refers to the work-function for specific instrument and material. The BE is unique for each electron level of each element. The binding energy and intensity of a photoelectron peak gives information about the elemental identity, chemical state and quantity of the element. The electrons originating from a few atomic layers below the surface contribute to the analysis, hence making it a surface sensitive technique. Typical analysis depth is around 3 to 10 nm. Depending on the amount of elements present, photo cross-section and electron attenuation length, numbers of electrons are proportionally detected.

In the present study, XPS was carried out on nanopowder using a PHI 5500 instrument (Physical Electronics, Chanhassen, Minnesota, USA) for surface chemical analysis. This instrument is equipped with a monochromatic AlK_α (1486.6 eV, photon energy) X-ray source. Ultra-high vacuum conditions of 10^{-9} mbar were maintained during the powder analysis. The X-ray source and the spectrometer form an angle of 90° with one another making an angle of 45° with the sample surface normal. For survey scan, 93.9 eV pass energy and 0.4 eV/step were used and high resolution XPS was performed for elements of interest by using 23.5 eV pass energy and 0.1 eV/step. High resolution XPS (HR XPS) provides oxide and metal intensities which could be used to evaluate the shell oxide thickness. Before the measurements, energy calibration was carried out using pure elemental standards of Au, Ag and Cu. The etching was performed using argon gas with an accelerating voltage of 4 kV. A raster scan by Ar^+ beam over 4 x 5 mm^2 to 2 x 3 mm^2 area gave an etch rate of 3 to 5 nm min^{-1}. The etch rate was calibrated on a flat Ta_2O_5 foil of known thickness (100 nm), thus the oxide thickness refers to Ta_2O_5 units, which is expected to be of the same order of magnitude as that of Fe-oxide [55]. Samples for XPS analysis were prepared inside the glove box. Loose powder was mounted on a double sided adhesive conductive carbon tape. In the present study, iterated Shirley type background correction was applied as it is essential to remove the peaks from an inelastic scattering background and asymmetric components were assigned for area integration.

4.2.5 **Electron Microscopy**

Scanning electron microscope (SEM) uses a focused beam of electrons, which impinge on a sample surface and generate a variety of signals. Information on the topography, atomic number contrast, chemical composition, crystal orientation can be derived from the signals generated due to the interaction of the electrons with the sample. In SEM, an electron source (can be W/LaB6 filament or field emission gun) emits high energy electrons that are directed on to the specimen. These electrons carry significant amounts of kinetic energy and when they hit the sample, this energy is dissipated as a variety of signals during the interaction. The interaction depth varies between 1 to 5 µm. The different signals are secondary electrons, backscattered electrons, diffracted backscattered electrons and photons. Secondary electrons are used for topographic imaging, while the backscattered electrons are used for illustrating contrast in composition for multiphase samples [56]. X-ray generation due to the inelastic collisions

between the incident and sample electrons can be used to analyze the chemical composition of the sample using energy dispersive spectroscopy (EDS). The energy of the electron beam typically ranges from 1 to 40 kV. A typical SEM consists of an electron source, electron lenses to focus the electron beam on to specimen, sample stage, detectors for the signals of interest, output devices and vacuum systems. The SEM is considered to be one of the most versatile techniques in the study of solid materials.

In the present study, SEM was used to compliment the results from XPS, analyze the mixing homogeneity and fractography of sinter compacts. A high resolution scanning electron microscope (HRSEM), LEO Gemini 1550 (CARL ZEISS – LEO electron microscope, GmbH, Germany) equipped with field emission gun was used to perform the microscopy analysis. The imaging was performed using an in-lens detector as it provides high resolution and improved topological contrast at low beam voltages. This is for imaging the features which are in the order of a few hundred nanometers.

4.2.6 **Optical Microscopy and Density Measurement**

Optical microscopy (OM) is a technique which uses light in the visible spectrum to image the topography or phase composition/feature contrast of a sample. It is mostly useful for features of sizes down to the micron range. For the metals, the sample surface has to be reflective in nature for the OM. For the same purpose, the samples of interest were mounted in a conducting resin (Ployfast by Struers) using a hot mounting machine (Citopress-20, Struers). Grinding and polishing was carried out to prepare the sample surface to mirror like surface. After specimen preparation, OM was carried out using an optical microscope (Leitz DMRX, Leica).

Density measurements were carried out on green and sintered compacts to see the difference in density due to the sintering process. For the green compacts, the density was evaluated by measuring the mass and volume of the sample using a simple balance of 0.0001 g accuracy and conventional measuring tools, respectively. The Archimedes' principle based density determination kit from OHAUS was used to measure density of sintered samples.

5 Summary of the appended papers

For easier understanding, the results have been divided into two parts: Powder characterization and sintering studies.

5.1 Powder characterization

Surface characteristics of the micro-powder ASC 300 (-45 µm) was studied in detail by Wendel et al. [57]. Small oxide particulates enriched in Mn, Cr and Si in the order of less than 100 nm were observed on the surface. The XPS study revealed that the surface iron oxide was around 6 to 7 nm in thickness and there was minor presence of Mn, Cr and Si in oxide state on the powder surface. Auger electron spectroscopy (AES) confirmed that the scarce particulate oxides were rich in Mn and Cr. When sintered at 1350 °C, the surface was devoid of any such particulate oxides. Therefore, it could be said that the sintering temperature and atmosphere were sufficient for the removal of all kinds of oxides. Thermogravimetry (TGA) results revealed that the oxide reduction occurred in steps. At first, around 400 °C, the iron oxide layer was reduced. After this there was a continuous mass loss related to reduction of surface oxide particulates and also internal oxides.

The following subsections details about the surface characteristics and thermal behavior of nanopowder, respectively.

5.1.1 Surface Characterization (Paper 1)

X-ray photoelectron spectroscopy (XPS) was used for surface characterization of nanopowder. Nanopowder was expected to have a core-shell structure which means that metal core is covered by an oxide shell. The aim was to calculate the thickness of this oxide shell. Both iron and steel nanopowder were subjected to XPS for the same purpose. The TG was used to complement and validate the results obtained from XPS. Below is the summary of the findings from XPS and TG.

XPS

Survey scan from 0 to 1100 eV binding energy (BE) was carried out on the prepared sample surface and it revealed the presence of elements in the near surface region of the powder (Figure 12). Peaks at 711, 640 and 530 eV were observed which represents the presence of iron, manganese and oxygen respectively. The iron peak represents both metallic and oxides of iron. Therefore, HR XPS was carried out to differentiate the content of different states. In the case of iron nanopowder, metallic signal was observed on the surface. This was absent in the case of steel nanopowder. Different models were used to fit the data from XPS in order to calculate the oxide thickness.

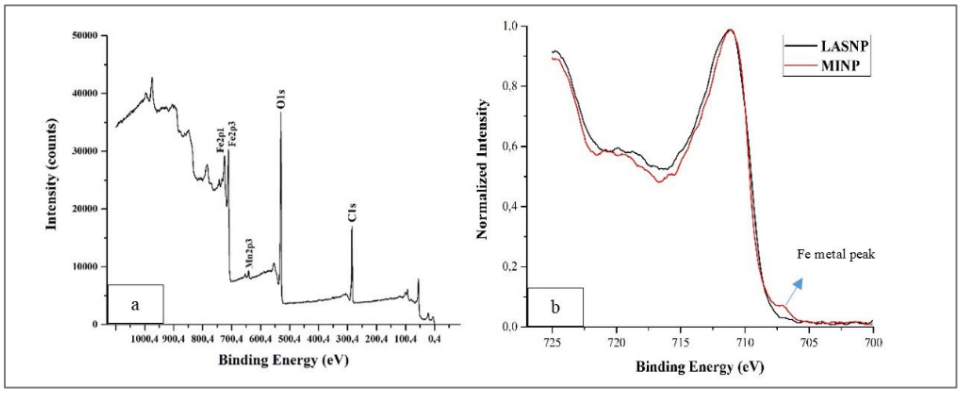

Figure 12: (a) survey scan on the surface of iron nanopowder, (b) HR XPS peaks of Fe2p3 for iron and steel nanopowder.

The first approach uses relationship between average escape depth factor and ratio between oxide thickness and electron mean free path [58].

$$t^{ox}/\lambda^{ox} = (cos\theta)_s ln[1 + \frac{I^{ox} I^{m}_{\infty}}{I^{ox}_{\infty} I^{m}}] \quad \textbf{Equation 5}$$

Where t^{ox} is oxide thickness, λ^{ox} is electron mean free path in the oxide, $(cos\theta)_s$ is average escape depth factor, I^m and I^{ox} are intensities of metal and oxide respectively, and I^m_∞ and I^{ox}_∞ are intensities of infinitely thick metal and oxide, respectively. Intensities obtained from the surface are used as an input. Therefore, this was used only for iron nanopowder but not for steel nanopowder. Using this approach, Eq. 5, values of 3.15, 3.45 and 3.45 nm were obtained for 35-45, 40-60 and 60-80 nm iron nanopowder, respectively.

The second approach uses depth profile technique and integration of the region under the curve for the metallic and oxide peaks. This is repeated at every depth and a plot is done showing Fe metal intensity vs. etch depth. Thickness of the oxide is estimated to be the depth at which 0.65 metallic intensity is achieved [58], based on model taking into account powder shape, predicted range of oxide thickness, etch rate and electron attenuation length. Through this method, thickness of the oxide was estimated to be 8.5, 8.5 and 6.1 nm for 35-45, 40-60 and 60-80 nm iron nanopowder, respectively. This approach was also used for steel nanopowder and the thickness was calculated to be around 15 nm. This approach clearly overestimates the thickness of the oxide scale due to the fact that the appearance of metallic signal on the surface indicating otherwise, showing that XPS depth profiling is not a consistent method for core-shell structures of nanopowder.

The third approach is a planar surface approach [59] where geometric correction was done for spherical shape using XPS Multiquant software [60] [61].

$$d = Ï_{ox} cos\alpha ln\left(\frac{N_{me} Ï_{me} I_{ox}}{N_{ox} Ï_{ox} I_{me}} + 1\right) \quad \textbf{Equation 6}$$

where I_{me} is the photoelectron intensity of the metal and I_{ox} the photoelectron intensity of the oxide, while N_{me} and N_{ox} are the number of atoms per unit volume in the metal and oxide, respectively and $Ï$ is the attenuation length. Photoelectron intensity of metal and oxide measured from the HR XPS scan on the surface of the powder was used for I_{me} and I_{ox}, respectively. Using Eq. 6, the thickness of the oxide is measured to be 4.0, 4.1 and 4.1 nm for 35-45, 40-60 and 60-80 nm iron nanopowder, respectively, on the assumption that the surface can be viewed as flat projection. As the nanopowder particles have curved topography, the above values have to be corrected [62]. This correction was done using XPS Multiquant software and the thickness was found to be 2.7, 3.0 and 2.9 nm for 35-45, 40-60 and 60-80 nm iron nanopowder, respectively. This approach was only used for iron but not steel nanopowder because of the absence of metallic signal from the original surface of the powder.

Last approach using XPS data was the one proposed by A.G. Shard which is a simple and a straightforward method to determine the thickness of oxide by taking into account the metallic and oxide intensity from the surface [63].

$$T_{NP} = \frac{T_{R\sim1} + \beta T_0}{1+\beta} \quad \textbf{Equation 7}$$

Where $T_{R\sim1}$ is given by using the radius of the particle, overlay thickness on a planar sample and multiplying with a geometrical correction term or topofactor [64]. The factor β is a function of photoelectron intensity, photoelectron kinetic energy, attenuation lengths and the effective

atomic number of the components involved and T_0 represents the thickness calculation for infinitesimally small particles. Using Eq. 7, the oxide thickness was calculated to be approximately 2.9, 2.8 and 2.8 nm for 35-45, 40-60 and 60-80 nm metal particles, respectively. Even this approach was not suitable for steel nanopowder due to the absence of metallic signal from the original surface.

TG and surface area correlation

TG analysis was carried out on iron nanopowder and a mass loss of 6.9, 6.8 and 4.6 % was observed in 35-45, 40-60 and 60-80 nm iron nanopowder, respectively. These values along with surface area values were used in Eq. 8 to calculate the oxide thickness:

$$t_{scale} = \frac{\Delta m}{BET\ X\ \rho_{scale}\ X\ 0.3} \qquad \textbf{Equation 8}$$

where t_{scale} is the thickness of oxide scale (cm), Δm is the percentage mass loss from TG, *BET* is the surface area (cm^2/g) of nanopowder and ρ is the density (g/cm^3) of the scale. A factor of 0.3 is used to account for the oxygen mass fraction in the iron oxide. The calculated thickness was 2.5, 3.0 and 3.0 nm for 35-45, 40-60 and 60-80 nm iron nanopowder respectively.

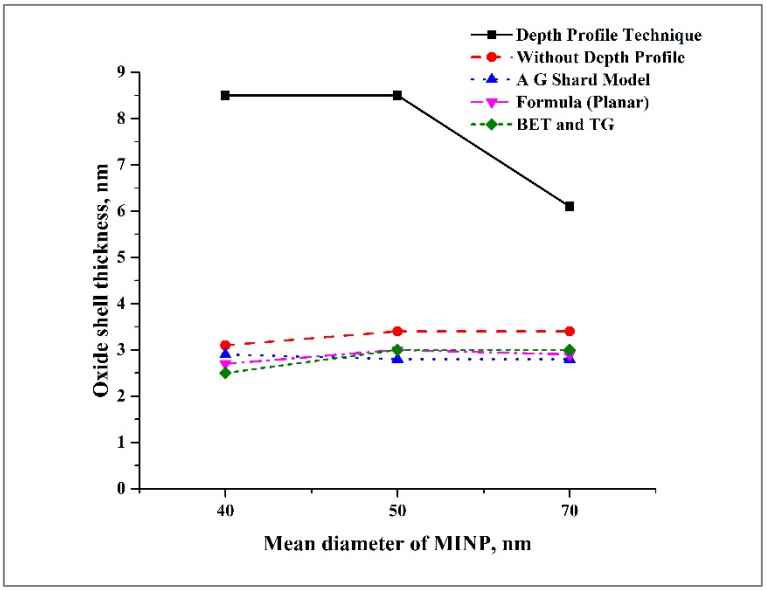

Figure 13: Thickness of oxide scale calculated using different models.

It can be said from the above results that except for the depth profile approach all the other approaches were in agreement with one another and an oxide thickness value of around 3 nm was calculated on the iron nanopowder (Figure 13). The passive layer measured on iron when exposed to air at room temperature is also 3 nm in thickness. The oxide scale on steel nanopowder through depth profile approach was measured to 15 nm but this method is not suitable for measuring the oxide thickness of nanopowder, although it can be assumed that this powder has greater oxide thickness than 3 nm since no metal iron peak is shown when analyzing the original powder surface.

5.1.2 Thermal behavior of iron nanopowder

To explain the melt point depression for nano particles, a classical thermodynamics approach was adopted by the use of Gibbs-Thomson equation [38]

$$T_m(r) = T_m(\infty) - \frac{2T_m(\infty)\sigma_{sl}}{\Delta H_f(\infty)\rho_s r} \quad \textbf{Equation 9}$$

where $T_m(\infty)$ is the melting temperature of the bulk material, $\Delta H_f(\infty)$ is the latent heat of fusion of the bulk material, ρ_s is the density of the material in solid state, r is the radius of the particle, $T_m(r)$ is the melting temperature of a particle with radius r and σ_{sl} is the solid-liquid interfacial energy. The shape of the particle is assumed to be spherical in shape. This equation is a simple way of predicting a relationship between the melting point temperature and decreasing particle size. It could be said that this was used to describe the behavior of low melting materials like low molecular weight organic liquids, cadmium or polymer lamella crystals [38]. A modified version of Gibbs-Thomson equation for size-dependent melt point depression is given by the following:

$$\left(\frac{T_m(r)}{T_m(\infty)}\right)^C = 1 - C\frac{2\sigma_{sl}}{\Delta H_f(\infty)\rho_s r} \quad \textbf{Equation 10}$$

Where $C = T_m(\frac{\rho_s}{(\rho_s - \rho_l)})(\alpha_{ls} - \alpha_s)$, ρ_l is the density in liquid state and α_{ls} & α_s are the co-efficients of thermal expansion in both the phases. This form of the equation is valid for shallow depressions or for values of C not very high. A C-value of 1.04 was reported for Al. There are other models to predict the melting point dependence on the particle size [38]. One other model used for the prediction is based on the liquid film which forms on the particle surface. The equation is modified for liquid-skin model, where a thin liquid skin surrounds the solid particle [65]. Though this model is not suitable for metals particles like aluminum and iron as they are coated with an oxide passivation layer.

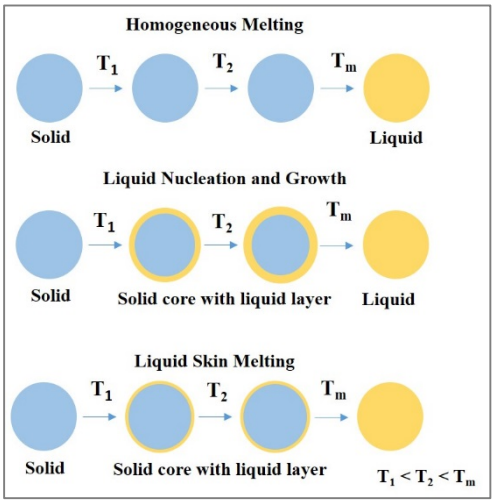

Figure 14: Different melting hypotheses for nanoparticles (Redrawn from [36]**).**

There are different melting processes as shown in Figure 14. The first one, homogenous melting is that the entire solid is in equilibrium with the melted particles. There is no surface melting involved in this case [39]. The T_m in the above figure represents the melting point of the nanoparticles.

The melting point through this mechanism can be calculated using the following equation:

$$\frac{T_m}{T_M} = 1 - \frac{4V}{\Delta H_f D}\left[\gamma_{sv} - \gamma_{lv}\left(\frac{\rho_s}{\rho_l}\right)^{\frac{2}{3}}\right] \quad \textbf{Equation 11}$$

where γ_{sv} is the surface energy of solid-vapour interface, γ_{lv} is the surface energy of liquid-vapour interface, T_M is the bulk melting temperature, ΔH_f is the bulk heat of fusion, D is the diameter of the nanoparticles, ρ_s is the density of the solid and ρ_l is the density of the liquid.

When the liquid layer nucleates at the surface and grows with temperature in to the solid core to eventually become complete liquid, such a mechanism is called liquid nucleation and growth and the equation changes to [66]:

$$\frac{T_m}{T_M} = 1 - \frac{6V}{\Delta H_f D}\left[\gamma_{sv} - \gamma_{lv}\left(\frac{\rho_s}{\rho_l}\right)^{\frac{1}{2}}\right] \qquad \textbf{Equation 12}$$

The last of the three is liquid skin melting model where a liquid layer is formed over the solid core at temperature lower than the melting temperature and remain unchanged till the particles transforms completely to liquid at the melting temperature [67]. The melting temperature is given by:

$$\frac{T_m}{T_M} = 1 - \frac{4V\gamma_{sl}}{\Delta H_f (D-2\delta)} \qquad \textbf{Equation 13}$$

The Eqs. 11 and 12, which represent the homogenous melting and liquid nucleation and growth model follow a linear variation between melting temperature and the inverse particle size. The decrease in the melting temperature does not depend linearly with the inverse particle size in the case of liquid skin melting model.

In the present work, Gibbs-Thomson equation was used to calculate the melting point of the iron nanopowder used for the study. The nanopowder of interest had a size range from 35 to 80 nm. The calculation yielded values close to the bulk melting point temperature. Therefore, the size of nanopowder in the present research is expected to be too large for the melt point depression to happen.

The melting behavior of the iron nanopowder was evaluated using differential scanning calorimeter (DSC) STA449 (NETZSCH Thermal Analysis GmbH, Germany). All the experiments were performed in argon atmosphere and a flow rate of 50 ml/min was used. Final target temperature of 1450 °C was employed with a heating rate of 10 °C/min. Alumina pans with lid were used for measurement. A mass of around 100 to 120 mg was used and a heating rate of 10 °C/min was employed.

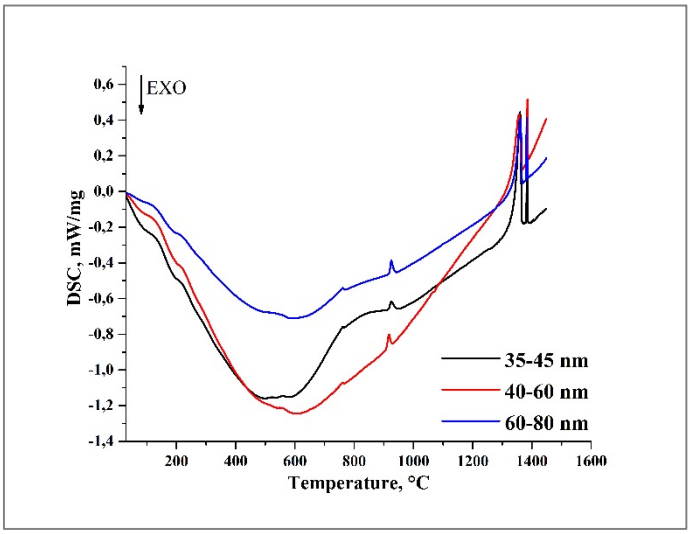

Figure 15: DSC curves of iron nanopowder in all three size fractions.

The endothermic peaks observed around 900 and 1400 °C correspond to the allotropic transformations of BCC Fe to FCC Fe (α to γ) and FCC Fe to BCC Fe (γ to δ) respectively. An additional endothermic peak at was observed at 1365 °C (Figure 15). The energy absorbed for this transformation was higher than the energy absorbed for the allotropic transformations. In agreement with the Gibbs-Thomson calculations which predicted that the melt point temperature of the powder in the interested size range is equal to the bulk melting temperature, it cannot hence be concluded that the peak at 1365°C is related to the melt formation. The additional peak observed at around 1365°C disappeared in the DSC curves of powder blends. It is not clear what this endothermic peak corresponds to as it was observed only in the nanopowder samples.

There is a possibility for the nanopowder to not melt but to sinter and form a sinter mass. The reason can be that the size of the nanoparticles may be bigger than the one required for melt point depression to occur. Therefore the melting point of such powder is same as that of the bulk melting point. Therefore, from sintering perspective, it is important to study the surface oxide reduction as it influences the extent of sintering.

This section of the present study aims at understanding the reaction kinetics of spherical iron nanopowder with an oxide shell during hydrogen reduction.

Evaluation of the reduction kinetics of iron nanopowder in hydrogen atmosphere

One of the most important parameter to evaluate the reduction of the surface oxide is by evaluating the apparent activation energy [68]. This depends largely on factors like raw material, reducing agent, temperature range, impurities, and physical shape [69]. There are different methods used to evaluate the apparent activation energy, using model fitting and iso-conversional methods [70], [71]. To use iso-conversional methods, experiments at different heating rates are carried out. In this method, conversion fraction of the reaction is expressed as following

$$\boldsymbol{\alpha = \frac{\omega_i - \omega}{\omega_i - \omega_f}} \qquad \textbf{Equation 14}$$

where ω_i, ω and ω_f are the initial, actual and final weight of the sample, respectively. The rate of the reaction from fraction of the reaction is described as:

$$\boldsymbol{\frac{d\alpha}{dt} = \beta \frac{d\alpha}{dT} = k(T) f(\alpha) = A exp\left(\frac{-E}{RT}\right) f(\alpha)} \qquad \textbf{Equation 15}$$

where α is the conversion fraction of the reaction, β is the heating rate employed, $k(T)$ is the rate constant for temperature T and $f(\alpha)$ is a function of α. The A and E are the pre-exponential and activation energy, respectively, and R is the universal gas constant.

There are different methods like Friedman (FR) method [72], Nonlinear Vyazovkin (NLV) method [73] and Kissinger-Akahira-Sunose (KAS) method [74], [75], generally used for the interpretation of E in iso-conversional evaluation of apparent activation energy. Out of the three methods, the KAS method is the mostly commonly or widely used as it is more accurate than the FR method and the values obtained are comparable to those of the NLV method. The FR method is considered to be less accurate for low and high values of α as it is very sensitive to experimental noise and numerically unstable [68]. The NLV method is considered to be a complex process owing to the complex computations as part of the method. In KAS method the above equation changes to:

$$\boldsymbol{ln\left(\frac{\beta}{T^2}\right) = -\frac{E}{RT} + ln\left(\frac{AE}{g(\alpha)R}\right)} \qquad \textbf{Equation 16}$$

where T is the temperature at transformation, $g(\alpha)$ is the integral from Eq. 16 and $ln\left(\frac{AE}{g(\alpha)R}\right)$ is a parameter independent of transformation temperature and heating rate. This equation represent y=mx+c expression as when α is constant, that is considering the conversion fraction is constant, the plot between $ln\left(\frac{\beta}{T^2}\right)$ versus $\frac{1}{T}$ yields a straight line and whose slope is used to arrive at the activation energy (E). This expression has been used in the present study to calculate the apparent activation energy.

To investigate the surface oxide reduction, thermogravimetric analysis was performed using a simultaneous thermal analyzer STA449 (NETZSCH Thermal Analysis GmbH, Germany). A small alumina crucible was used as a vessel for the sample to be analyzed. Crucible along with the sample was placed in the middle of the vertical furnace on top a thermocouple pole. A sample size of around 200±5 mg was used and hydrogen atmosphere was used for the reduction process. Before the commencement of the experiment, the furnace tube was evacuated and purged with argon gas for three times. All the samples were heated to 1350°C with a heating rate of 10, 30 and 50 °C/min. A constant flow of hydrogen gas at 100 ml/min was maintained throughout the experiment.

Figure 16 shows the result of TG measurements heated to 1350°C in hydrogen atmosphere at different heating rates. The total mass loss was observed to be 7.2 to 7.8, 6.5 to 6.8 and 4.5 to 5 % for 35-45, 40-60 and 60-80 nm iron nanopowder. This mass corresponds to the value of iron oxide present on the nanopowder. A thickness of 3 nm of oxide scale has been found on the nanopowder [76] and is safe to say that it has been completely reduced at the end of the experiment. The thickness is same on all the size fractions, the difference is from the difference in the surface area between the different size fractions. With an increase in heating rate the complete reduction process shifts to higher temperature. It was not very clear from the TG curves if the reduction was one step or multiple steps. Therefore, the TG data was differentiated against temperature and plotted in differential thermogravimetric curves (DTG). It can be seen from Figure 16 that 2 different peaks were observed in the case of nanopowder of 60-80 nm size fraction and these curves shifted depending on the heating rate. Different peaks, one at T<200 °C and the other at T<650 °C were observed at higher heating rates like 30 and 50 °C/min. For the one with 10 °C/min, the peak at higher temperature was only clear at T<600 °C. Similar phenomenon was observed in the other size fractions, except that the temperature was on the lower side compared to that for the 60-80 nm size fraction. The first peak varied from 150 to 175 °C, whereas the second one occurred at between 400 to 600 °C. The first peak corresponds to the loss of passive layer over the nanopowder which helps in minimizing the agglomeration and may also partly be due to the moisture loss. The second peak corresponds to the oxide reduction and also accounts for almost all of the mass loss. Higher heating rate not only shifted the peaks to higher temperature but also broadened the peaks by increasing the total time taken for the reaction to complete.

To understand the reduction behavior of surface iron oxide in nanopowder, apparent activation energy calculations were carried out using KAS method. Using Eq. 16 iso-conversional plot of $ln\left(\frac{\beta}{T^2}\right)$ versus $\frac{1}{T}$ was plotted for all the three size fractions (Figure 17). Linear fit was made and the slope was used to calculate apparent activation energy by multiplying with universal gas constant (-R). Plot showing the activation energy is Figure 17. The activation energy for the surface oxide reduction was found to be in the range of 40 to 80 kJ/mol with an increasing activation energy value for increasing size. It is known from literature that the activation energy required for the conversion of oxide to Fe is in the range of 15-172 kJ/mol [68]. During the reduction of iron oxide using hydrogen, it was found that the activation energy values associated

with the two-step reduction process of Fe_2O_3 to Fe_3O_4 and then subsequently to metallic Fe had values of 90 and 70 kJ/mol [77] while using Arrhenius plot.

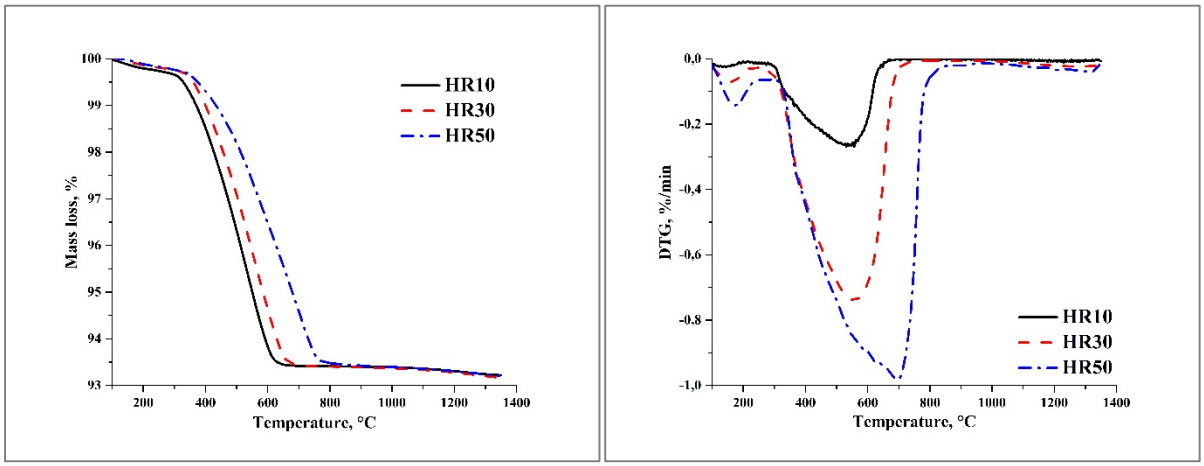

Figure 16: TG and DTG curves for 60-80 nm iron nanopowder.

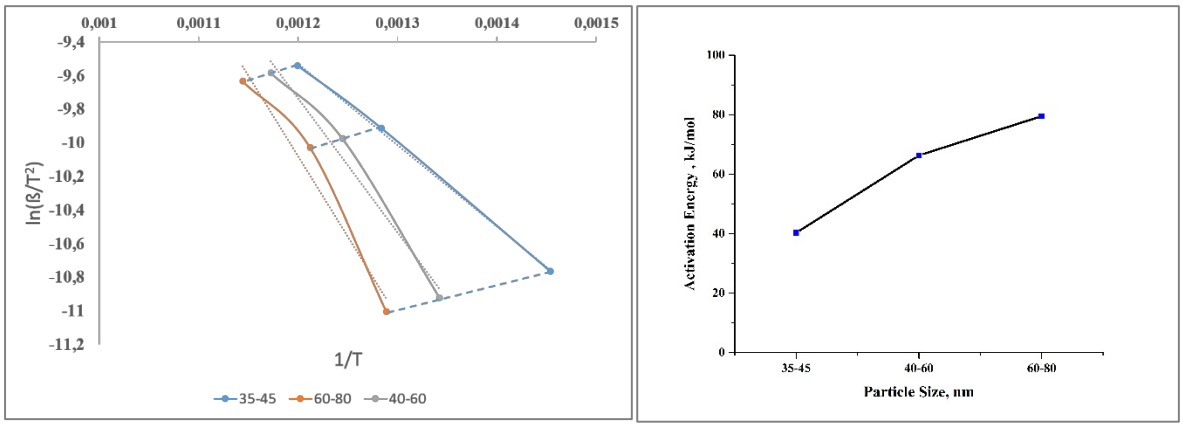

Figure 17 Activation energy estimations for the reduction of surface oxide in iron nanopowder.

5.2 Results from compaction and sintering (Papers 2 & 3)

5.2.1 Compaction

Different powder blends were compacted and the compatibility curves are shown in Figure 18. It is apparent that increase in compaction pressure increases the green density. Compacts with addition of iron nanopowder showed good compressibility. Presence of graphite decreased the green density at higher compaction pressures. At low compaction pressure, it acts as lubricant and helps to achieve high green density. Compacts with steel nanopowder have lower green density in comparison with that of compacts with iron nanopowder. Presence of nanopowder influences the compressibility of the powder and was found to decrease the green density [43]. For the compacts containing only micro-powder, the green density was approximately 7.35 g/cm^3 when compacted at 800 MPa [11]. When 5 wt% nanopowder content was employed the green density got reduced to 7.3 g/cm^3. The compressibility decreased with an overall increasing nanopowder content in the powder blend (Figure 18). It was shown from the study using SEM and electron backscatter diffraction (EBSD) that compacts produced at higher compaction pressures (like 800 MPa) exhibited severely deformed structure near the particle edges for the ASC 300 (-45 µm) particles [11]. In the present case, this deformed region can be spread across the nanosized particles because of their size and can influence the sintering.

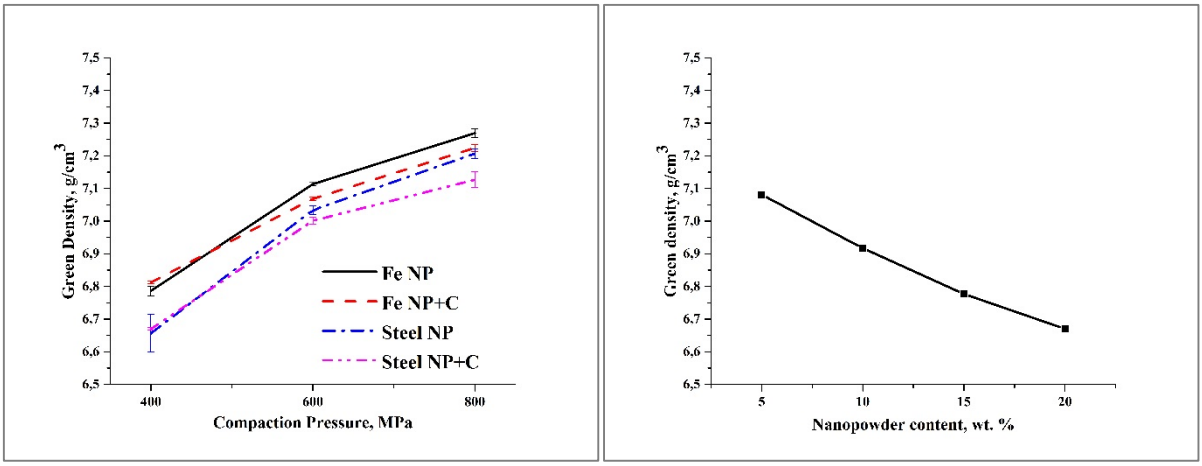

Figure 18: Compressibility curves of (a) varying composition and compaction pressure (Paper 2) and (b) varying amounts of iron nanopowder.

5.2.2 Sintering

5.2.2.1 Addition of nanopowder

On sintering the green compacts with iron nanopowder at 1350 °C, shrinkage was increased from 1 to 1.5 % when the compaction pressure increased from 400 to 800 MPa (Figure 19). Presence of carbon along with nanopowder increased the shrinkage from 1.6 to 2.2 % when the compaction pressure increased (Figure 19). When steel nanopowder was used shrinkage was more or less the same at 1.5 % for all the compaction pressures but when carbon was added it changed from 1.5 to 2.2 % when the pressure increased (Figure 20). Different heating rates were employed for sintering and the influence on the overall shrinkage was negligible. There was a shift in the on-set of the α to γ transformation temperature with an increasing heating rate (Figure 21).

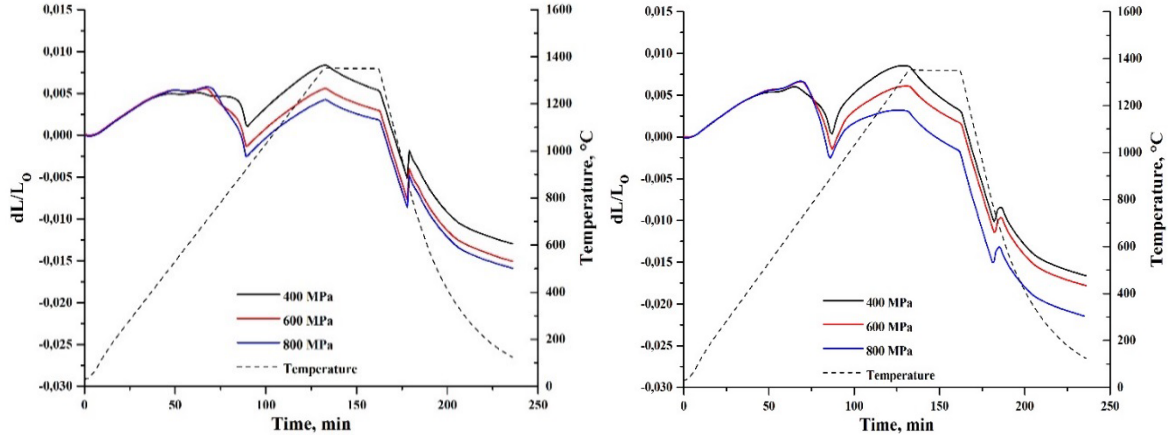

Figure 19: Sintering curves showing powder blend compacts with 5 wt. % of (a) iron nanopowder and (b) iron nanopowder with graphite (Paper 2).

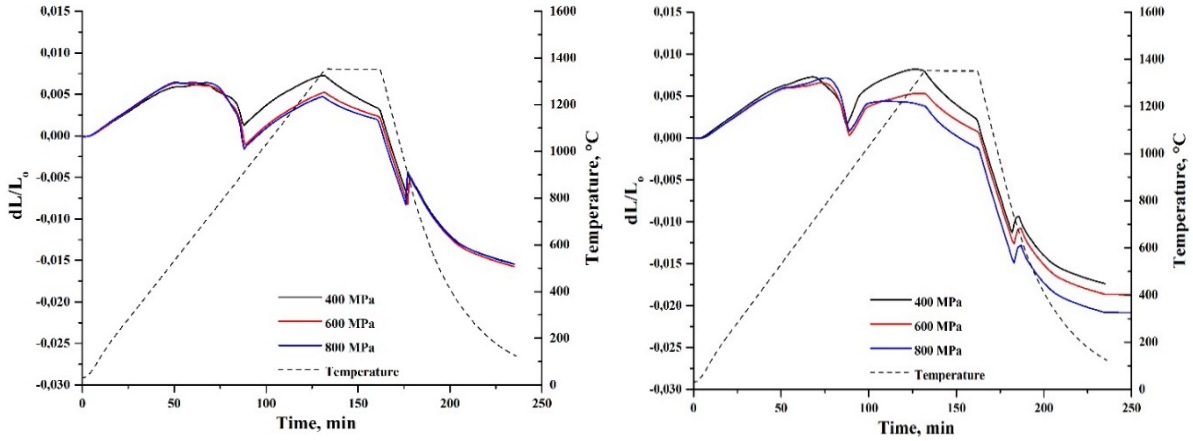

Figure 20: Sintering curves showing powder blend compacts mixed with 5 wt. % of (a) steel nanopowder and (b) steel nanopowder with graphite (Paper 2).

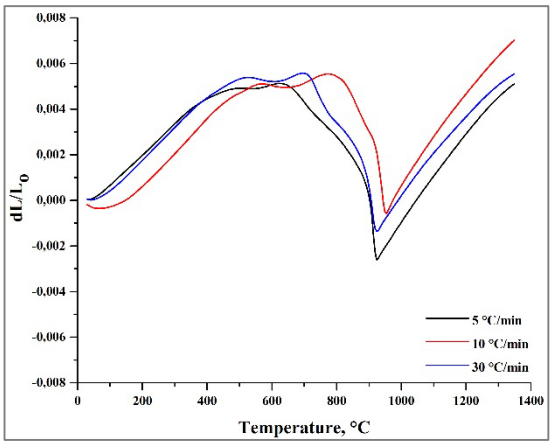

Figure 21: Influence of heating rate on the on-set of the ferrite to austenite transition (Paper 2).

To understand the influence of nanopowder addition, the sinter behavior of nanopowder blend compact was compared to the compact with only micrometer sized powder (Figure 22). A clear

difference was observed between the two sinter curves though the nature of the curves was same. The compact with nanopowder underwent densification in the lower temperature range.

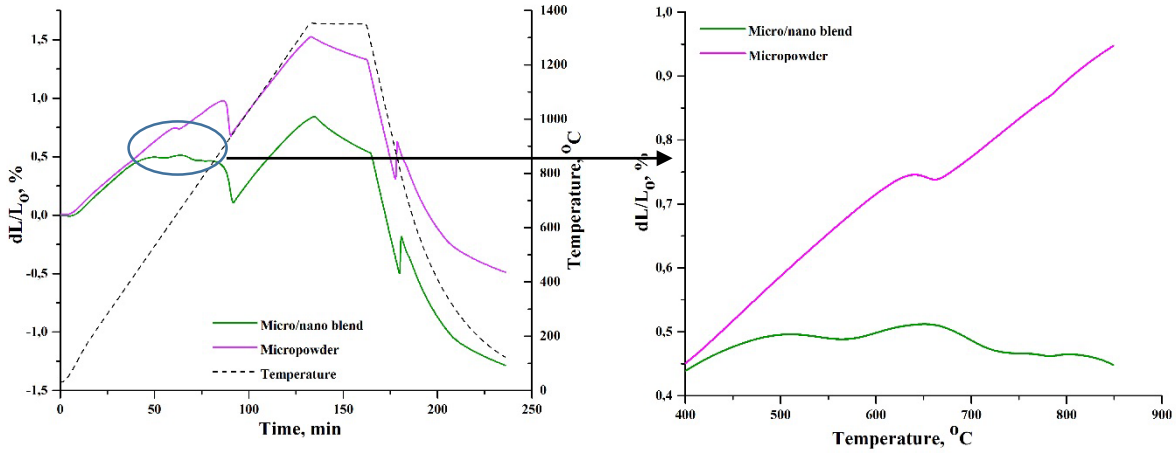

Figure 22: Sinter curves showing the influence of nanopowder addition (paper 2)

To analyse this difference, compacts with iron nanopowder were subjected to intermittent sintering at temperatures like 500, 700, 900 and 1100 °C (Figure 23).

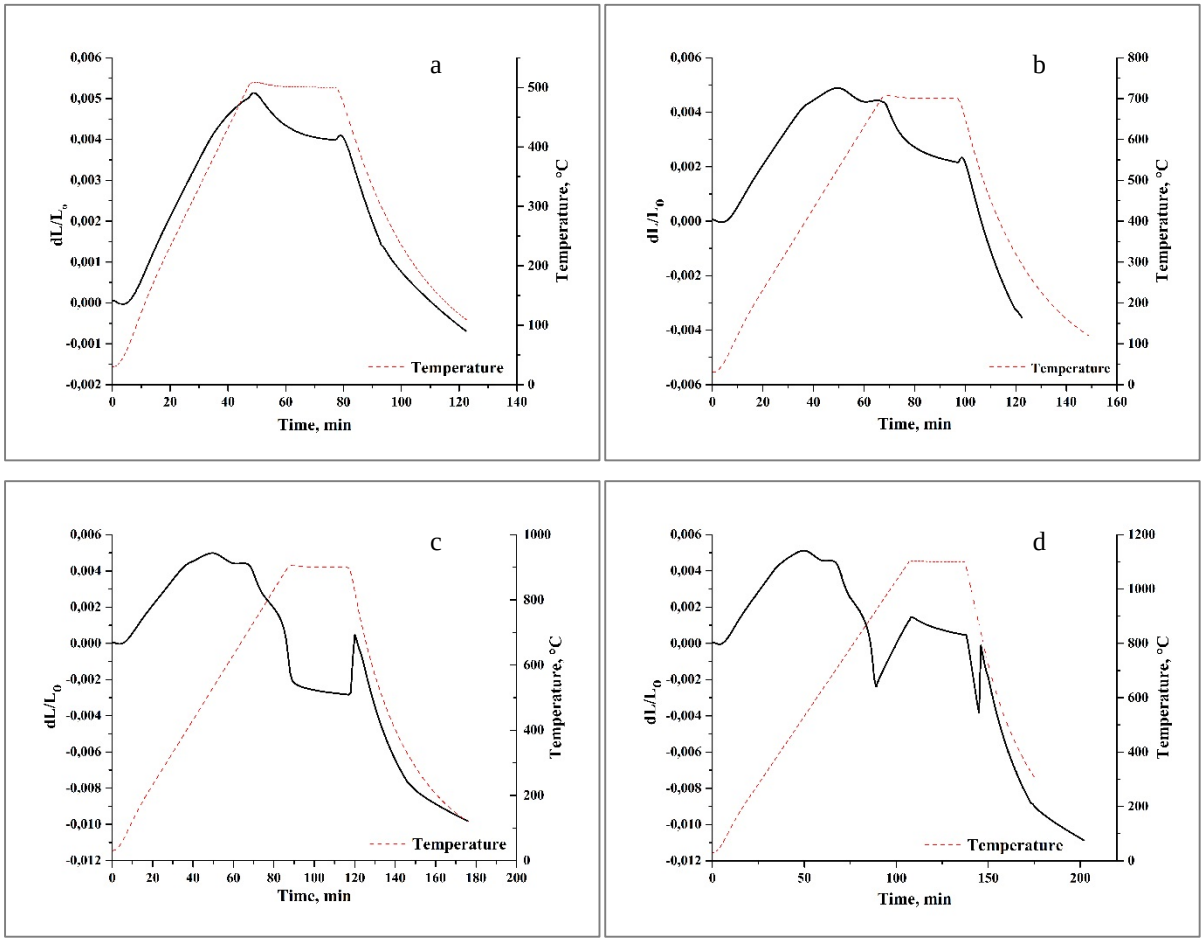

Figure 23: Sinter curves at intermittent sintering temperatures (a) 500, (b) 700, (c) 900 and (d) 1100 °C.

The sintered compacts were subjected to fractography to evaluate the difference in sintering behavior (Figure 24). It is clear that the nanopowder was sintered at between 500-700 °C from the fractographs; at 500 °C nanopowder retains its shape and size, while at 700 °C clear

sintering of nanopowder was observed. This could be related to the reduction of nanopowder surface oxide between 500-700°C obtained from thermogravimetric data. Also, it was observed that the surface oxide scale is reduced at 400 °C for the micropowder [57]. At 900 °C, no nanopowder was observed (Figure 24). The nanopowder during sintering not only sintered to itself but also to the neighboring micrometer sized powder particle. This helps in increasing the contact area between the particles which in turn helps in densification. Hence, any individual effect of nanopowder providing melt depression (if any) at higher temperature should have been lost. Similar phenomenon was observed by Lee et al. for MIM system [35].

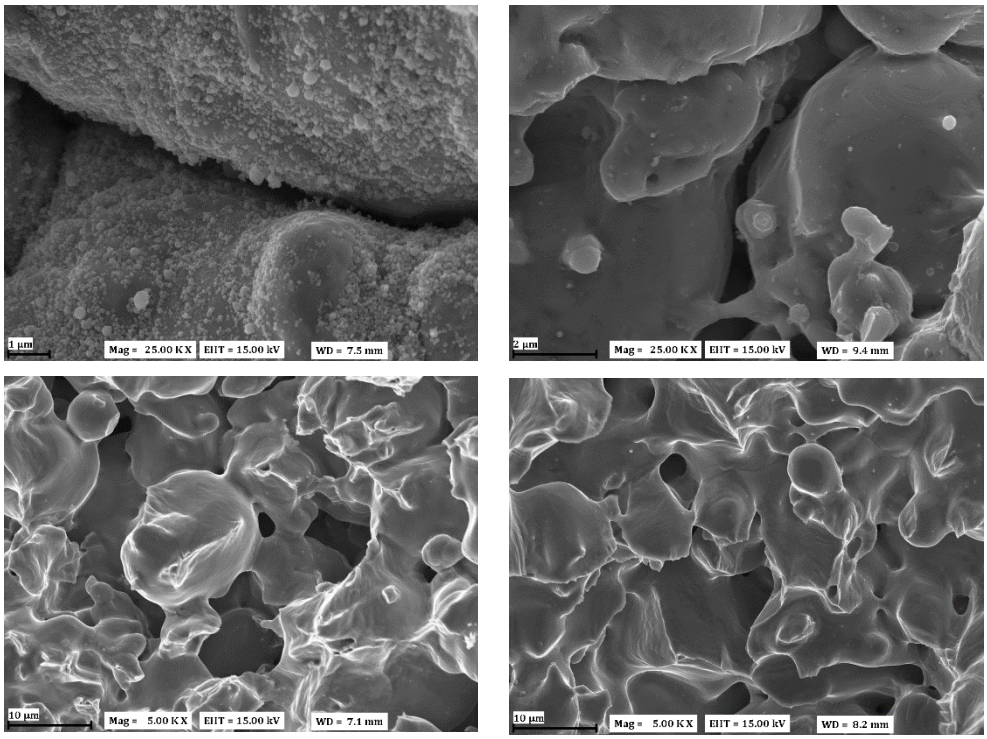

Figure 24: SEM Micrographs showing the fracture surface of sintered compact at temperature at (a) 500, (b) 700, (c) 900 and (d) 1100 °C.

Increasing the nanopowder content

Different amounts of iron nanopowder was added and its influence on sintering was studied. (From 5 to 20 wt.% nanopowder content). The shrinkage increased from 1.5 to 3.0 % when the nanopowder content was increased from 5 to 20%. The slope of the sintering curve turns steeper with an increasing nanopowder content. The behavior of the curves with different content changes above 500 °C (Figure 25). Activation with respect to nanopowder is triggered only above this temperature.

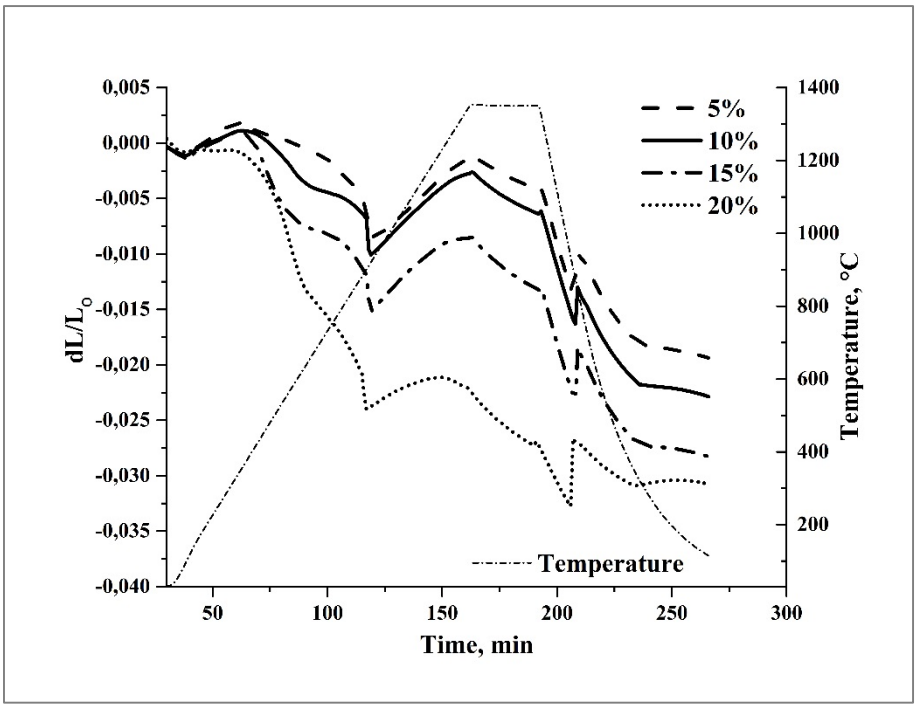

Figure 25: Sintering curves showing the influence of nanopowder content in the powder blend compact.

Sinter density and densification parameter

Sinter density increased with an increasing compaction pressure and the amount of nanopowder also influences the sinter density as depicted in Figure 26. Densification parameter was used to see the extent of densification and was calculated using the formula [78]:

$$\Psi = \frac{\rho_s - \rho_g}{\rho_t - \rho_g} \qquad \textbf{Equation 17}$$

where ρ_s is the sinter density, ρ_g is the green density and ρ_t is the theoretical density.

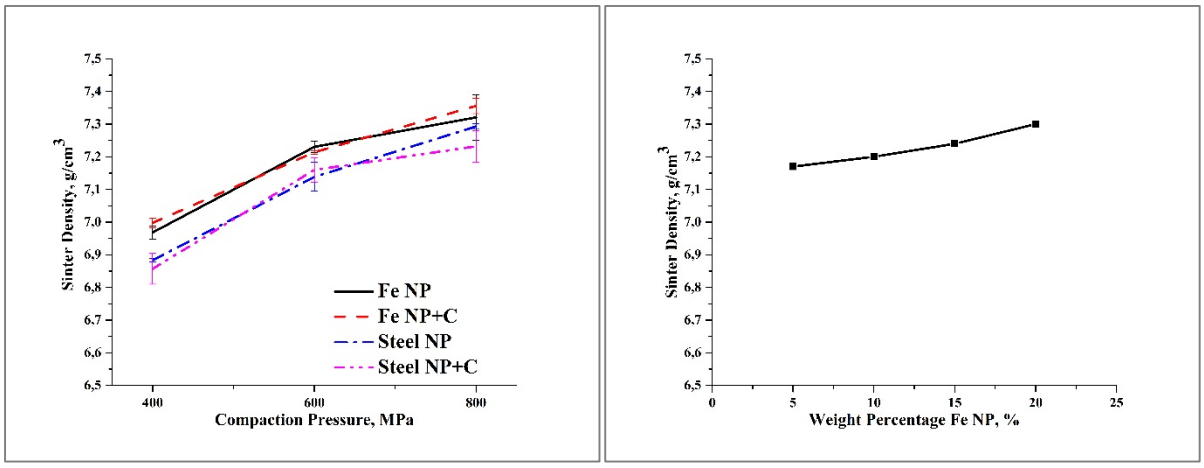

Figure 26: Graph showing (a) the influence of compaction pressure on the sinter density (b) Varying amount of nanopowder in the powder blend sintered at 1350°C for 0.5 h.

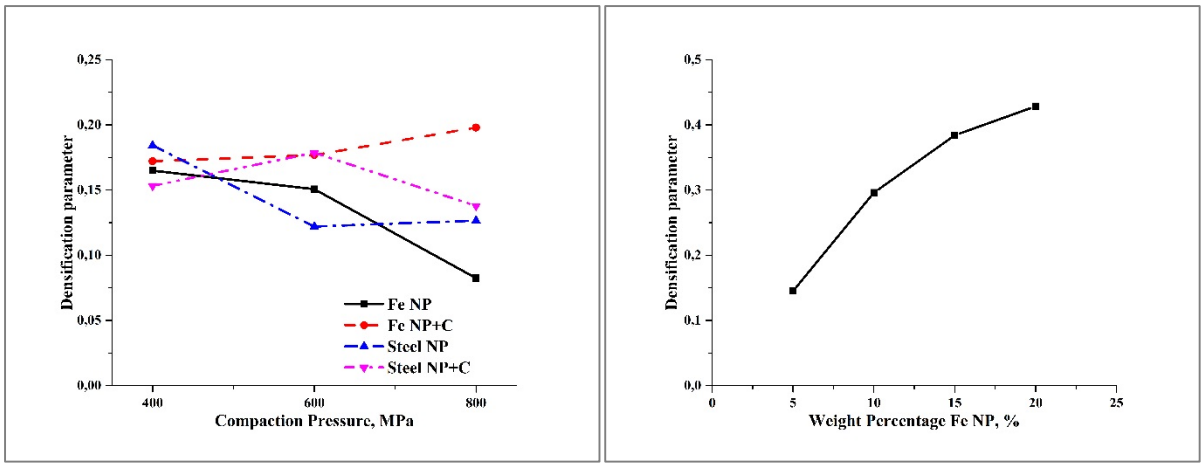

Figure 27: Densification parameter for sintered compacts (a) pressed at different compaction pressures and (b) varying amounts of nanopowder in the powder blend for 0.5 h at 1350 °C.

Figure 27 shows that densification parameter values. The results are complex with effects of compaction pressure on densification parameter values (Figure 27) indicatively being different for different kind of blends; still there is tendency that increased compaction pressure may depress the densification during sintering. Clear is, however, that densification parameter increases with an increase in nanopowder content (Figure 27).

6 Conclusions

The findings of the present thesis study shed light on following issues.

1. Surface oxide thickness measurement of iron nanopowder
    - Different models were used to evaluate the XPS data and a methodology to measure the thickness of surface oxide on nanopowder was established.
    - All the models except the depth profiling technique yielded an oxide thickness of approximately 3 nm for the size fractions of iron nanopowder.
    - The XPS results were in agreement with the calculations made through TGA-surface area correlation.
    - For the case of steel nanopowder, thicker oxide scale well above 3 nm over the surface is expected owing to the manufacturing process; the lack of metal signal from the surface making it difficult for evaluation using available core-shell models and only XPS depth profiling is possible, but not recommended as it provides lack of precision for nanopowder

2. Activation energy calculations for surface oxide reduction of nanopowder
    - The activation energies for oxide scale reduction in iron nanopowder were calculated using Kissinger equation.
    - The DSC curves revealed only phase transition peaks but no clear melting peaks for iron nanopowder.
    - Gibbs Thompson calculations corresponding to the melt-point depression for iron nanopowder suggested the lack of occurrence of melting below that for bulk metal even for the size range below 10 nm.
3. Influence of the powder blend constituents on the compressibility
    - The presence and increase in nano powder content decreased the compressibility of the blends proportionally to the content
    - At lower compaction pressures, graphite improved the green density but decreased the green density when higher pressures were applied.
4. Influence of nano powder on the sintering behavior
    - The presence of nanopowder imparted shrinkage in the compacts observable significantly already at temperatures of 500 to 700 °C.
    - An increase in the content of nanopowder increased the sintered density of the compacts proportionally with the nanopowder content.

7 Future work

The present study has addressed the use of iron nanopowder as the model powder to evaluate the influence of such addition on the sintering of water-atomized iron powder. This knowledge serves as a basis to try experimenting with different alloy nanopowder in next stage. The surface characterization methodology developed in the present study can be used for the evaluation of surface oxide of different alloy nanopowder which would be helpful in developing the sintering of different powder blends. Different alloy systems can be explored in order to have a low melting point temperature and use such systems to promote liquid phase sintering in addition to the observed low temperature sintering enhancement. The integration of carbon source is expected to be an important means also for further studies.

Extensive DSC, XRD and advanced characterization techniques like XPS, TEM are to be used to study next stage design of nanopowder addition. A more in-depth analysis to study the diffusion behaviour of tailored nanopowder and to see how this helps in achieving liquid phase like sintering when added to water atomised iron powder should be considered.

To study sintering by using nanopowder agglomerates instead of nanopowder can also be explored.

On the application front, gear blank manufactured out of powder blend is close to realisation. The intention is to use the powder blend, compact through cold isostatic compaction (CIP) and high temperature sintering to reach closed porosity compacts, with and without nanopowder additions.

Acknowledgements

I would like to thank my supervisor and examiner Prof. Lars Nyborg for providing me with an opportunity to carry out research at the department of industrial and materials science. I would also like to thank Prof. Eduard Hryha, my co-supervisor for providing guidance and support.

I would like to acknowledge Swedish Foundation for Strategic Research for funding this project.

I would like to thank Dr. Dimitris Chasoglou and Mr. Dmitri Riabov at Höganäs for the support in regard to powder supply and compaction. I would like to mention Prof. Johan Liu and Mr. Hafid for the collaboration with regard to nano additives. Johan Wendel for all the help, collaboration and conversations about powder.

I would like to thank Dr. Ruslan Shvab and Assoc. Prof. Yu Cao for their help with surface characterization. I would like to thank Dr. Eric Tam, Dr. Yiming Yao and Roger Saghdahl for all the help and fixing things for us.

I would like to take this opportunity and thank Dr. T. K. Nandy, Mr. Abhay K. Jha and Dr. Ramesh Narayanan for introducing me to the world of materials research. Special thanks to NPTEL.

I would like to thank my colleagues at the department of industrial and materials science for creating and maintaining a pleasant environment. Special thanks to my past and present officemates, Giulio and Mahesh for keeping the office space ‘loud’ and lively. My buddies at work Adrianna, Elangho, Sukhdeep and Dinesh for the interesting discussions.

I would like to thank my friends Ajay, Sharmista and Vishnu for making Sweden home away from home. My battery of cousins and friends back home-I miss you all! My parents and Karthik, my brother for supporting and encouraging me. Seshendra, for being yourself!

References

[1] *Höganäs Handbook for Sintered Components-3. Design and Properties*. Höganäs AB, 2004.

[2] "Economic Considerations for Powder Metallurgy Structural Parts." [Online]. Available: https://www.pm-review.com/introduction-to-powder-metallurgy/economic-considerations-for-powder-metallurgy-structural-parts/. [Accessed: 29-Oct-2018].

[3] K. H. Roll and P. K. Johnson, "Iron Powder Metallurgy Spearheads Industry Growth," *Iron Powder Metall.*, pp. 1–7, 1968.

[4] W. D. Kingery, "Sintering from Prehistoric Times to the Present," in *Sintering '91*, 1992, vol. 25, pp. 1–10.

[5] P. Ramakrishnan, "History of Powder Metallurgy," *Indian J. Hist. Sci.*, vol. 18, no. 1, pp. 109–114, 1983.

[6] F. G. Hanejko, "Warm compaction," in *ASM Handbook Powder Metal Technologies and Applications*, vol. 7, 1998, pp. 376–381.

[7] "European Powder Metallurgy Association (EPMA) - Powder Manufacture." [Online]. Available: https://www.epma.com/powder-metallurgy-powder-manufacture. [Accessed: 29-Oct-2018].

[8] K. Skotnicová, M. Kursa, and I. Szurman, *Powder Metallurgy*. 2014.

[9] E. Peter and W. Lee, "ASM Handbook: Volume 7: Powder Metal Technologies and Applications," 1st ed., vol. 7, P. Ed and L. W, Eds. ASM International, 1998, p. 1147.

[10] "Powder production - LPW Technology." [Online]. Available: https://www.lpwtechnology.com/technical-library/powder-production/. [Accessed: 30-Oct-2018].

[11] J. Wendel, "Characteristics and Sintering of Fine Water-atomized and Carbonyl Iron Powder Characteristics and Sintering of Fine Water-atomized and," Chalmers University of Technology, 2018.

[12] "Power Metallurgy - Advantages and Limitations." [Online]. Available: https://www.eit.edu.au/cms/resources/technical-resourses/power-metallurgy-advantages-and-limitations. [Accessed: 27-Oct-2018].

[13] "Powder Metallurgy Advantages: Why Use Powder Metallurgy? | PickPM." [Online]. Available: https://www.pickpm.com/introduction-powder-metallurgy/advantages-powder-metallurgy/. [Accessed: 27-Oct-2018].

[14] A. Panda, J. Dobransky, M. Jancik, I. Pandova, and M. Kacalova, "ADVANTAGES AND EFFECTIVENESS OF THE POWDER," *METALURGIJA*, vol. 57, no. 4, pp. 353–356, 2018.

[15] "Why Powder Metallurgy?" [Online]. Available: https://www.pm-review.com/introduction-to-powder-metallurgy/why-powder-metallurgy/. [Accessed: 27-Oct-2018].

[16] "Powder Metallurgy | Process, Advantages, Disadvantages, Applications." [Online]. Available: https://clubtechnical.com/powder-metallurgy. [Accessed: 26-Oct-2018].

[17] "Powder Metallurgy Process with its Advantages and Disadvantages - mech4study." [Online]. Available: http://www.mech4study.com/2017/05/powder-metallurgy-

process.html. [Accessed: 31-Oct-2018].

[18] "Design Considerations with Powder Metallurgy | PickPM." [Online]. Available: https://www.pickpm.com/design-resource-center/design-considerations/. [Accessed: 30-Oct-2018].

[19] R. M. German, *Sintering: From Empirical Observations to Scientific Principles*. 2014.

[20] R. M. German, P. Suri, and S. J. Park, "Review: Liquid phase sintering," *J. Mater. Sci.*, vol. 44, no. 1, pp. 1–39, 2009.

[21] R. M. German, *Sintering Theory and Practice*. New York: John Wiley & Sons, 1996.

[22] J. K. Mackenzie and R. Shuttleworth, "A phenomenological theory of sintering," *Proc. Phys. Soc. Sect. B*, vol. 62, no. 12, pp. 833–852, 1949.

[23] E. A. Olevsky, "Theory of sintering: from discrete to continuum," *Mater. Sci. Eng. R*, vol. 23, pp. 41–100, 1998.

[24] F. A. Nichols, "Theory of sintering of wires by surface diffusion," *Acta Metall.*, vol. 16, no. 1, pp. 103–113, 1968.

[25] H. Djohari and J. J. Derby, "Transport mechanisms and densification during sintering: II. Grain boundaries," *Chem. Eng. Sci.*, vol. 64, no. 17, pp. 3810–3816, 2009.

[26] H. Djohari, J. I. Martínez-Herrera, and J. J. Derby, "Transport mechanisms and densification during sintering: I. Viscous flow versus vacancy diffusion," *Chem. Eng. Sci.*, vol. 64, no. 17, pp. 3799–3809, Sep. 2009.

[27] J. H. Dedrick and A. Gerds, "A study of the mechanism of sintering of metallic particles," *J. Appl. Phys.*, vol. 20, no. 11, pp. 1042–1044, 1949.

[28] R. L. Coble, "Sintering crystalline solids. I. intermediate and final state diffusion models," *J. Appl. Phys.*, vol. 32, no. 5, pp. 787–792, 1961.

[29] R. L. Coble, "Sintering crystalline solids. II. experimental test of diffusion models in powder compacts," *J. Appl. Phys.*, vol. 32, no. 5, pp. 793–799, 1961.

[30] R. M. German, "Chapter Six - Geometric Trajectories during Sintering," in *Sintering: from Empirical Observations to Scientific Principles*, R. M. German, Ed. Boston: Butterworth-Heinemann, 2014, pp. 141–181.

[31] "NPTEL :: Metallurgy and Material Science - Advanced ceramics for strategic applications." [Online]. Available: https://nptel.ac.in/courses/113105015/. [Accessed: 02-Nov-2018].

[32] R. M. German, "Coarsening in Sintering: Grain Shape Distribution, Grain Size Distribution, and Grain Growth Kinetics in Solid-Pore Systems," *Crit. Rev. Solid State Mater. Sci.*, vol. 35, no. 4, pp. 263–305, 2010.

[33] C. You, C. Luan, and X. Wang, "An evaluation of solid bridge force using penetration to measure rheological properties," *Powder Technol.*, vol. 239, pp. 175–182, 2013.

[34] O. Dominguez, Y. Champion, and J. Bigot, "Liquidlike Sintering Behavior of Nanometric Fe and Cu Powders: Experimental Approach," *Metall. Mater. Trans. A Phys. Metall. Mater. Sci.*, vol. 29, no. 12, pp. 2941–2949, 1998.

[35] J.-P. Choi, H.-G. Lyu, W.-S. Lee, and J.-S. Lee, "Densification and microstructural development during sintering of powder injection molded Fe micro–nanopowder," *Powder Technol.*, vol. 253, pp. 596–601, 2014.

[36] K. K. Nanda, “Size-dependent melting of nanoparticles: Hundred years of Thermodynamic model,” *Pramana - J. Phys.*, vol. 72, no. 4, pp. 617–628, 2009.

[37] P. P, “Ober die Abhängigkeit des Schmelzpunktes von der Oberflächenenergie eines festen Körpers (Zusatz.),” *Zeitschrift für Physikalische Chemie*, vol. 65U. p. 545, 1909.

[38] J. Sun and S. L. Simon, “The melting behavior of aluminum nanoparticles,” vol. 463, pp. 32–40, 2007.

[39] P. Buffat and J.-P. Borel, “Size effect on the melting temperature of gold particles,” *Physic Al Rev. a Vol.*, vol. 13, no. 6, pp. 2287–2298, 1976.

[40] P. Couchman and W. A. Jesser, “Thermodynamic theory of size dependence of melting temperature in metals,” *Nature*, vol. 270, no. December 15, p. 572, 1977.

[41] P. Jena, B. K. Rao, and S. N. Khanna, *The Physics and Chemistry of Small Clusters*, vol. B158. New York: Plenum Press, 1987.

[42] J. R. Groza, “Nanosintering,” *Nanostructured Mater.*, vol. 12, no. 5, pp. 987–992, 1999.

[43] O. Dominguez, M. Phillippot, and J. Bigot, “The relationship between consolidation behavior and particle size in Fe nanometric powders,” *Scr. Metall. Mater.*, vol. 32, no. 1, pp. 13–17, 1995.

[44] J. Rajabi, N. Muhamad, and A. B. Sulong, “Effect of nano-sized powders on powder injection molding: a review,” *Microsyst. Technol.*, vol. 18, no. 12, pp. 1941–1961, Dec. 2012.

[45] J. W. Oh, R. Bollina, W. S. Lee, and S. J. Park, “Effect of nanopowder ratio in bimodal powder mixture on powder injection molding,” *Powder Technol.*, vol. 302, pp. 168–176, 2016.

[46] Y. S. Kang, B. H. Cha, H. G. Kang, and J. S. Lee, “Densification behavior and microstructural development of nano-agglomerate powder during sintering,” *Mater. Sci. Forum*, vol. 534–536, no. 1, pp. 505–8.

[47] J. W. Oh, S. K. Ryu, W. S. Lee, and S. J. Park, “Analysis of compaction and sintering behavior of 316L stainless steel nano/micro bimodal powder,” *Powder Technol.*, vol. 322, pp. 1–8, 2017.

[48] D. Wei, R. Dave, and R. Pfeffer, “Mixing and Characterization of Nanosized Powders: An Assessment of Different Techniques,” *J. Nanoparticle Res.*, vol. 4, no. 1, pp. 21–41, Apr. 2002.

[49] J. Fruhstorfer, S. Schafföner, and C. G. Aneziris, “Dry ball mixing and deagglomeration of alumina and zirconia composite fine powders using a bimodal ball size distribution,” *Ceram. Int.*, vol. 40, no. 9, Part B, pp. 15293–15302, 2014.

[50] F. Persson, A. Eliasson, and P. G. Jönsson, “Oxidation of Water Atomized Metal Powders,” *steel Res. Int.*, vol. 85, no. 12, pp. 1629–1638.

[51] L. Nyborg, T. Tunberg, and P. X. Wang, “Surface product formation during water atomization and sintering of austenitic stainless steel powder,” *Met. Powder Rep.*, vol. 45, no. 11, pp. 750–753, 1990.

[52] P. J. Haines, “Thermogravimetry,” in *Thermal Methods of Analysis: Principles, Applications and Problems*, Dordrecht: Springer Netherlands, 1995, pp. 22–62.

[53] H. Bhadeshia, “Dilatometry.” [Online]. Available: https://www.phase-

trans.msm.cam.ac.uk/2002/Thermal3.pdf. [Accessed: 15-Oct-2018].

[54] “X-Ray Photoelectron Spectroscopy (XPS) Surface Analysis Technique.” .

[55] R. Simpson, R. G. White, J. F. Watts, and M. A. Baker, “Applied Surface Science XPS investigation of monatomic and cluster argon ion sputtering of tantalum pentoxide,” *Appl. Phys. Lett.*, vol. 405, pp. 79–87, 2017.

[56] “Scanning Electron Microscopy (SEM).” .

[57] J. Wendel, R. Shvab, Y. Cao, E. Hryha, and L. Nyborg, “Surface analysis of fine water-atomized iron powder and sintered material,” 2018.

[58] L. Nyborg, A. Nylund, and I. Olefjord, “Thickness Determination of oxide layers on spherically-shaped metal powders by ESCA,” *Surf. Interface Anal.*, vol. 12, pp. 110–114, 1988.

[59] M. Mohai and I. Bert, “Calculation of overlayer thickness on curved surfaces based on XPS intensities,” *Surf. Interface Anal.*, vol. 36, pp. 805–808, 2004.

[60] M. Mohai, *XPS Multiquant Users Manual*. 2005.

[61] M. Mohai, “XPS MultiQuant : multimodel XPS quantification software,” *Surf. Interface Anal.*, vol. 2, no. 36, pp. 828–832, 2004.

[62] J. E. Martin *et al.*, “Determination of the Oxide Layer Thickness in Core - Shell Zerovalent Iron Nanoparticles,” *Langmuir*, vol. 24, no. 3, pp. 4329–4334, 2008.

[63] A. G. Shard, “A Straightforward Method For Interpreting XPS Data From Core −shell nanoparticles,” *J. Phys. Chem. Chysical Chem. C*, vol. 116, pp. 16806–16813, 2012.

[64] A. G. Shard, J. Wang, and S. J. Spencer, “XPS topofactors : determining overlayer thickness on particles and fibres,” *Surf. Interface Anal.*, vol. 41, pp. 541–548, 2009.

[65] M. Zhang *et al.*, “Size-dependent melting point depression of nanostructures: Nanocalorimetric measurements,” *Phys. Rev. B*, vol. 62, no. 15, pp. 10548–10557, 2000.

[66] S. C. Hendy, “A thermodynamic model for the melting of supported metal nanoparticles,” *Nanotechnology*, vol. 18, no. 17, 2007.

[67] C. R. M. Wronski, “The size dependence of the melting point of small particles of tin,” *Br. J. Appl. Phys.*, vol. 18, no. 12, pp. 1731–1737, 1967.

[68] G. Y. Lee, J. ll Song, and J. S. Lee, “Reaction kinetics and phase transformation during hydrogen reduction of spherical Fe2O3nanopowder agglomerates,” *Powder Technol.*, vol. 302, pp. 215–221, 2016.

[69] A. Pineau, N. Kanari, and I. Gaballah, “Kinetics of reduction of iron oxides by H2. Part II. Low temperature reduction of magnetite,” *Thermochim. Acta*, vol. 456, no. 2, pp. 75–88, 2007.

[70] M. E. Brown *et al.*, “Computational aspects of kinetic analysis: Part A: The ICTAC kinetics project-data, methods and results,” *Thermochim. Acta*, vol. 355, no. 1, pp. 125–143, 2000.

[71] A. Khawam and D. R. Flanagan, “Role of isoconversional methods in varying activation energies of solid-state kinetics: II. Nonisothermal kinetic studies,” *Thermochim. Acta*, vol. 436, no. 1–2, pp. 101–112, 2005.

[72] H. L. Friedman, “Kinetics of thermal degradation of char-forming plastics from

thermogravimetry. Application to a phenolic plastic," *J. Polym. Sci. Part C Polym. Symp.*, vol. 6, no. 1, pp. 183–195, 2007.

[73] S. Vyazovkin and D. Dollimore, "Linear and nonlinear procedures in isoconversional computations of the activation energy of nonisothermal reactions in solids," *J. Chem. Inf. Comput. Sci.*, vol. 36, no. 1, pp. 42–45, 1996.

[74] H. E. Kissinger, "Reaction Kinetics in Differential Thermal Analysis," *Anal. Chem.*, vol. 29, no. 11, pp. 1702–1706, 1957.

[75] S. Vyazovkin, *Isoconversional kinetics of thermally stimulated processes*. 2015.

[76] S. K. Manchili *et al.*, "Surface analysis of iron and steel nanopowder," *Surf. Interface Anal.*, no. March, pp. 1083–1088, 2018.

[77] H.-Y. Lin, Y.-W. Chen, and C. Li, "The mechanism of reduction of iron oxide by hydrogen," *Thermochim. Acta*, vol. 400, no. 1, pp. 61–67, 2003.

[78] S. Patra, Gouthama, and K. Mondal, "Densification behavior of mechanically milled Cu–8at% Cr alloy and its mechanical and electrical properties," *Prog. Nat. Sci. Mater. Int.*, vol. 24, no. 6, pp. 608–622, 2014.